BUBBLE MODELS AND DECOMPRESSION COMPUTATIONS: A REVIEW

B.R. Wienke
Nuclear Weapons Technology/Simulation And Computing
Applied And Computational Physics Division
C & C Dive Team Leader
Los Alamos National Laboratory
Los Alamos, N.M. 87545

ABSTRACT

A survey of bubble models in diving applications is presented, underscoring dual phase dynamics and quantifying metrics in tissue and blood. Algorithms covered include the multitissue, diffusion, split phase gradient, linear-exponential, asymmetric tissue, thermodynamic, varying permeability, reduced gradient bubble, modified gradient phase, tissue bubble diffusion, and linear-exponential phase models. Defining relationships are listed, and diver staging regimens are underscored. Implementations, diving sectors, and correlations are indicated for models with a history of widespread acceptance, utilization, and safe application across recreational, scientific, military, research, and technical communities. The past fifteen years, or so, have witnessed changes and additions to diving protocols and table procedures, such as shorter nonstop time limits, slower ascent rates, shallow safety stops, ascending repetitive profiles, deep decompression stops, helium based breathing mixtures, permissible, reverse profiles, multilevel techniques, both faster and slower controlling repetitive tissue halftimes, smaller critical tensions, longer flying-after-diving surface intervals, and others. Stimulated by Doppler and imaging technology, table and decompression meter development, theory, statistics, chamber and animal testing, or safer diving concensus, these modifications affect a gamut of activity, spanning bounce to decompression, single to multiday, and air to mixed gas diving. As it turns out, there is growing support for these protocols on operational, experimental, and theoretical grounds, with bubble models addressing many concerns on plausible bases and further testing or profile data bank analyses requisite.

Submitted – Undersea And Hyperbaric Medicine
Pages – 47, Tables – 6, Figures – 5, References – 92
Correspondence – B.R. Wienke, LANL, MS-F699, Los Alamos, N.M. 87545

Introduction

Gas exchange, bubble formation and elimination, and compression-decompression in blood and tissues are governed by many factors, such as diffusion, perfusion, phase separation and equilibration, nucleation and cavitation, local fluid shifts, and combinations thereof. Owing to the complexity of biological systems, multiplicity of tissues and media, diversity of interfaces and boundary conditions, and plethora of bubble impacting physical and chemical mechanisms, it is difficult to solve the decompression problem *in vivo*. Early decompression studies adopted the supersaturation viewpoint. Closer looks at the physics of phase separation and bubbles in the mid-1970s, and insights into gas transfer mechanisms, culminated in extended kinetics and dissolved-free phase theories. Integration of both approaches can proceed on the numerical side because calculational techniques can be made equivalent. Phase and bubble models are more general than supersaturation models, incorporating their predictive capabilities as subsets. Indeed, for most recreational and nonstop diving, bubble and dissolved gas models collapse onto themselves, that is, they suggest similar staging regimens.

Computational models gain efficacy by their ability to track data, often independently of physical interpretation. In that sense, the bottom line for computational models is utility, operational reliability, and reproducibility. Correct models can achieve such ends, but almost any model with sufficient parameter latitude might achieve those same ends. It is fair to say that deterministic models admit varying degrees of computational license, that model parameters may not correlate as complete set with the real world, and that not all mechanisms are addressed optimally. That is, perhaps, one reason why we see representative diving sectors, such as sport, military, commercial, and research, employing different tables, meters, models, and algorithms Yet, given this situation, phase models attempting to treat both free and dissolved gas exchange, bubbles and gas nuclei, and free phase trigger points appear preferable. Phase models have the right physical signatures, and thus the potential to likely extrapolate reasonably when confronting new applications and data. Expect to see their further refinement and development in the future.

Having said all that, data still plays the crucial role in model determination and applicability. Dive modeling is often more of an artform than science, and experiments directed at one or another aspect of unanswered diving questions can often produce divergent conclusions, further caveats, null results, and scattered-beyond-use data. Plus, macroscopic models cannot always cover all important aspects of microscopic phenomena. But they should not be at variance, either, with macroscopic observables. We do not cover data correlations herein. Instead we indicate range of model use, sector use, history, and some sources for data correlation. The intent here is to present a working view of physical phase mechanics, then followed by bubble model decompression theory in diving. Such discussion is neither medical nor physiological synthesis. Such aspects are omitted, and, for some, certainly oversimplified. This review updates and extends an earlier review [86] on dissolved gas models.

Model Backscapes

The physics, biology, engineering, physiology, medicine, and chemistry of diving center on pressure, and pressure changes. The average individual is subject to atmospheric pressure swings of 3% at sea level, as much as 20% a mile in elevation, more at higher altitudes, and all usually over time spans of hours to days. Divers and their equipment can experience compressions and decompressions orders of magnitude greater, and within considerably shorter time scales. While effects of pressure change are readily quantified in physics, chemistry, and engineering applications, the physiology, medicine, and biology of pressure changes in living systems are much more complicated. Caution is needed in transposing biological principles from one pressure range to another. Incomplete knowledge and mathematical complexities often prevent extensions of even simple causal relationships in biological science. With this, models of bubble formation in the body face a tough task.

The establishment and evolution of gas phases, and possible bubble trouble, involves a number of distinct, yet overlapping, steps [8,10,34,41,68,72,74,78]:

1. nucleation and stabilization (free phase inception);
2. supersaturation (dissolved gas buildup);
3. excitation and growth (free-dissolved phase interaction);
4. coalescence (bubble aggregation);
5. deformation and occlusion (tissue damage and ischemia).

The computational issues of bubble dynamics (formation, growth, and elimination) are mostly outside dissolved gas frameworks, but get folded into halftime specifications in a nontractable mode. The slow tissue compartments (halftimes large, or diffusivities small) might be tracking both free and dissolved gas exchange in poorly perfused regions. Free and dissolved phases, however, do not behave the same way under decompression. Care needs be exercised in applying model equations to each component. In the presence of increasing proportions of free phases, dissolved gas equations cannot track either species accurately. Computational algorithms tracking both dissolved and free phases offer broader perspectives and expeditious alternatives, but with some changes from classical schemes. Free and dissolved gas dynamics differ. The driving force (gradient) for free phase elimination increases with depth, directly opposite to the dissolved phase elimination gradient which decreases with depth. Then, changes in operational procedures are suggested for optimality. Considerations of excitation and growth invariably suggest deeper staging procedures than supersaturation methods.

Other issues concerning time sequencing of symptoms impact computational algorithms. That bubble formation is a predisposing condition for decompression sickness is universally accepted. However, formation mechanisms and their ultimate physiological effect are two related, yet distinct, issues. On this point, most hypotheses makes little distinction between bubble formation and the onset of bends symptoms. Yet we know that *silent* bubbles [7,8,67] have been detected in subjects not suffering from decompression sickness. So it would thus appear that bubble formation, per se, and bends symptoms do not map onto each other in a one-to-one manner. Other factors are operative, such as amount of gas dumped from solution, size of nucleation sites receiving the gas, permissible bubble growth rates, deformation of surrounding tissue medium, and coalescence mechanisms for small bubbles into large aggregates, to name a few. These issues are the pervue of bubble theories, but the complexity of mechanisms addressed does not lend itself easily to table, nor even meter, implementations. Difficulties accepted, model development and data correlation are ongoing efforts important in table fabrication, meter development, and dive planning software.

Cavitation And Nucleation

Simply, *cavitation* is the process of vapor phase formation [5,16,18,22,29,45,58] of a liquid when pressure is reduced. A liquid cavitates when vapor bubbles are formed and observed to grow as consequence of pressure reduction. When the phase transition results from pressure change in hydrodynamic flow, a two phase stream consisting of vapor and liquid results, called a cavitating flow [3,25,63]. The addition of heat, or heat transfer in a fluid, may also produce cavitation nuclei in the process called boiling. From the physico-chemical perspective, cavitation by pressure reduction and cavitation by heat addition represent the same phenomena, vapor formation and bubble growth, usually in the presence of seed nuclei. Depending on the rate and magnitude of pressure reduction, a bubble may grow slowly or rapidly. A bubble that grows very rapidly (explosively) contains the vapor phase of the liquid mostly, because the diffusion time is too short for any significant increase in entrained gas volume. The process is called vaporous cavitation, and depends on evaporation of liquid into the bubble. A bubble may also grow more slowly by diffusion of gas into the nucleus,

and contain mostly a gas component. In this case, the liquid degasses in what is called gaseous cavitation, the mode observed in the application of ultrasound signals to the liquid. For vaporous cavitation to occur, pressure drops below vapor pressure are requisite. For gaseous cavitation to occur, pressure drops may be less than, or greater than, vapor pressure, depending on nuclei size and degree of liquid saturation. In supersaturated ocean surfaces, for instance, vaporous cavitation occurs very nearly vapor pressure, while gaseous cavitation occurs above vapor pressure.

In gaseous cavitation processes, inception of growth in nuclei depends little on the duration of the pressure reduction, but the maximum size of the bubble produced does depend upon the time of pressure reduction. In most applications, the maximum size depends only slightly on the initial size of the seed nucleus. Under vaporous cavitation, the maximum size of the bubble produced is essentially independent of the dissolved gas content of the liquid. This obviously suggests different cavitation mechanisms for pressure (reduction) related bubble trauma in diving. Slowly developing bubble problems, such as limb bends many hours after exposure, might be linked to gaseous cavitation mechanisms, while rapid bubble problems, like central nervous system hits and and embolism immediately after surfacing, might link to vaporous cavitation. But it's certainly never been determined either way.

Now we know that the inception of cavitation in liquids involves the growth of submicroscopic nuclei containing vapor, gas, or both, which are present within the liquid, in crevices, on suspended matter or impurities, or on bounding layers [1,9,16,18,22,29,43,56,92]. The need for cavitating nuclei at vapor pressures is well established in the laboratory. There is some difficulty, however, in accounting for their presence and persistence. For a given difference between ambient and gas-vapor pressure, only one radius is stable. Changes in ambient, gas, or vapor pressures will cause the nuclei to either grow, or contract. But even if stable hydrostatically, bubbles and nuclei, because of constricting surface tension, will eventually collapse as gas and vapor diffuse out of the assembly. For instance, an air bubble of radius 10^{-3} cm will dissolve in saturated water in about 6 sec, and even faster if the water is undersaturated or the bubble is smaller. In saturated solutions, bubbles will grow by diffusion, and then tend to be quickly lost at free surfaces as buoyant forces raise them up. A 10^{-2} cm air bubble rises at the rate of 1.5 cm/sec in water. If nuclei are to persist in water, or for that matter, any liquid media, some mechanism must prevent their dissolution or buoyant exit.

A number of possibilities have been suggested to account for the presence of persistent, or stabilized, nuclei in undersaturated liquids, liquids that have been boiled, or denucleated. Crevices in the liquid, or surrounding boundary, may exert mechanical pressure on gas nuclei, holding them in place. Microscopic dust, or other impurities, on which gas and vapor are deposited, are stabilized already. Surface activated molecules, (such as hydrogen and hydroxyl ions in water), or surface activated skins formed from impurities may surround the nuclei and act as rigid spheres, offsetting constrictive surface tension, preventing diffusion of gas out of the nuclei and collapse. In all cases, the end result is a family, or group of families, of persistent nuclei. Time scales for stabilization and persistence of nuclei would obviously equate to the strength and persistence of stabilizing mechanism. Experimentally, trying to differentiate stabilization modes is difficult, because (eventual) growth patterns of nuclei are the same in all cases. The ultimate crumbling of surrounding shells, release of crevice mechanical pressure, removal of dust and impurity nucleation centers, and deactivation of surface chemicals can lead to the onset of bubble growth.

Flow Cavitation (Reynolds Nucleation)

Euler first studied cavitation in fluids, defining a cavitation number, κ. In a flowing fluid, the cavitation number, κ, is an indication of degree of cavitation, or tendency to cavitate [16,59,92]. Describing the similarity in the liquid-gas system, the cavitation number relates fluid pressure, p, to vapor pressure, p_ν, through,

$$\kappa = 2\,\frac{p - p_\nu}{\rho u^2}$$

with ρ and u the fluid density and velocity. Cavitation and cavitating flows have long been of interest

in shipbuilding and hydraulic machinery, underwater signal processing, propellor design, underwater detection, material damage, chemical processing, high pressure and temperature flows in nuclear reactors, volatility of rocket fuels, and bubble chambers for detection of high energy particles, to list a few. Cavitation processes in flowing blood and nearby tissue are of some interest to decompression modelers and table designers.

Any flow has a cavitation index, κ. If κ is very large, then p is sufficiently greater then p_ν and/or u is fairly small. In such cases, the Reynolds number, Re, with a the cavitation void radius, u stream velocity, and η fluid viscosity,

$$Re = \frac{\rho u a}{2\eta}$$

is small and single phase flow is the result. However, if u is increased, and/or p is decreased, nucleation will occur at some value, κ_i, denoted the *incipient cavitation index*. Cavitation will then occur in the flowing fluid provided,

$$\kappa \leq \kappa_i$$

At ambient pressure, at 20 ^oC, water has vapor pressure of roughly 0.03 atm. At 100 ^oC, water has vapor pressure of 1.00 atm and boils. Experiments peg the onset cavitation velocity of water near 15 m/sec, at 20 ^oC, permitting direct estimation of κ_i, Plugging the above values into the cavitation index equation, we find for water,

$$\kappa_i = 0.873$$

The density of water is a nominal 1.0 g/cm^3 above. If we consider water flowing at the same speed at 99 ^oC, with a vapor pressure of 0.99 atm, the cavitation index is roughly 100 times smaller, that is,

$$\kappa = 0.009$$

At 100 ^oC, the cavitation index is obviously zero (spontaneous boiling) for all flow speeds.

Certainly, the cavitation index, κ, is a more complicated function of flow parameters, Reynolds numbers, vapor pressure, and boundary conditions, but the above approach is extensively employed in calibrating cavitating flows. As the cavitation index drops further and further below the incipient value, bubble production increases. In the above, the vapor pressure, p_ν, is used, suggesting that the cavitation sites are filled with vapor. In reality, any combination of vapor and gas may fill the cavitation void, so the vapor pressure is replaced by p_c, the vapor-gas pressure,

$$\kappa = 2\,\frac{p - p_c}{\rho u^2}$$

The voids may indeed be filled with vapor, or backfilled with noncondensable wake gas just back of the cavitation site.

A number of notable cavitation patterns [16,45,58] breakout under flow cavitation and are of considerable interest to hydrodynamicists in high speed, high pressure flow regimes of propellors, airfoils and hydrofoils, turbine blades, pumps, reactor coolant flows, and fins, to name a few. Four generic cases (descriptors) are given below, but no connection with cavitation processes in the body is intimated nor linked therein:

1. *cloud cavitation* (periodic nucleation) – is a froathy structure resulting from the interaction of a driving blade or fin with the primary flow wake, and is periodic likely due to shielding of vortices in the wake, or some other periodic fluctuation induced in the flow, or embodied within the flow;

2. *sheet cavitation* (wake nucleation) – is a large scale cavitation carpet structure found on extended surfaces, resembles velour, and may be completely filled with vapor, and not necessarily a collection of individual bubbles;

3. *foil cavitation* (lift nucleation) – is another extended region of cavitation vapor, or gas, sitting on the lifting surface (top) of an airfoil, or hydrofoil, reducing lift, and often forming vortex cavitation ring structures at the foil juncture of upper and lower surfaces;

4. *vortex cavitation* (turbulence nucleation) – is a localized and focused, highly concentrated, vorticular cavitation bubble structure, often emanating from the sharp tips of propellors and fins in streamlines or rotating cascades, cause by pressure reductions within turbulent flow vortices.

Figure 1 is a photo montage of flow cavitation pictures taken with high speed underwater cameras. Reading left to right, and top to bottom, foil, cloud, sheet, and vortex cavitation are shown. From a modelers point of view, all but sheet cavitation are extremely difficult to simulate. From an engineers point of view, all cavitation processes in high speed flows are destructive and erosive on moving surfaces. When cavitation bubbles collapse, they fire out high speed shock waves in all directions, damaging surfaces and producing sharp sounds underwater. Modeling cavitation processes is tedious and intensive numerically.

Frictional Cavitation (Tribonucleation)

Tribonucleation has been demonstrated in the laboratory by Campbell and others [3,20,43,65], that is, a process in which solid contacting plates, immersed in a fluid, are separated very rapidly with the formation of voids and cavitation seeds. Upon separation of hydrophobic and hydrophilic surfaces, a bridging vapor cavity has been observed. In a fluid, dimensionally, one expects hydrostatic tension, τ, to depend on fluid viscosity, η, the velocity of separation, u, the cross sectional area of contacting surfaces, A, and inversely on a small separation volume, V, that is,

$$\tau = \zeta \frac{\eta u A}{V}$$

with ζ a (data fit) constant. Viscous adhesion is another term describing negative tension, τ, developed when hydrophobic surfaces are pulled apart. On circular plates, experiments suggest, with R plate radius, h plate separation, and $\zeta = 1$,

$$A \propto 4\pi R^2$$

$$V \propto \frac{4}{3}\pi h^3$$

so that,

$$\tau = 3\eta u \frac{R^2}{h^3}$$

Linking adhesion to cavitation, one might expect voids when,

$$p - \tau \leq p - p_\nu$$

for p fluid gas tension, or simply,

$$\tau \leq p_\nu$$

Negative tensions, τ, are generated easily, For instance, in nominal water at 20 ^oC, plates roughly 1 cm, separated at 0.1 mm, and pulled apart with a separation velocity of 1 cm/sec, produce a negative tension of 0.03 atm, in the vicinity of water vapor pressure.

Evans and Walder [30] showed that denucleated shrimp were more prone to bubble formation upon decompression if muscular contractions were performed before decompression. Harvey [36] demonstrated that damaged excised tissue was more susceptible to bubble formation than healthy tissue. In plate experiments in olive oil-glycerol-water fluids, Ikels [43] generated tribonuclei between both hydrophobic and hydrophilic bilayers. This suggests that cavities *in vivo* might be formed

by the rupture of cell membrane bilayers under exercise, as detailed by Powell [59]. Stress produced micronuclei in the body possibly occur with tissue surfaces coming together rapidly, and then withdrawing. Gas bubbles emerging from capillaries may have their genesis in the following way:

1. muscle contractions compress the capillary walls;
2. subsequent expansion of the capillary walls pushes back on muscle, changing dimensionality;
3. separation of the wall endothelium produces a void momentarily, with an inward flux of active oxygen, water vapor, and carbon dioxide gases tending to stabilize the hole;
4. when surrounding tissues are oversaturated with inert gas, the cavity experiences an ingassing gradient, and grows in size;
5. the initial hole is a (water) vaporous cavitation site, but later fills with gaseous components.

While such tribonucleation processes occur on time scales of seconds, the tribonuclei produced might last for hours, or so, depending on stabilization mechanisms offsetting constrictive surface tension. Also, the question of stabilization depends on the size of the tribonuclei, as very small ones might act like beebees and the large ones like soap bubbles under further muscle contraction-extension, gas loading, and tissue crevice shielding.

Radiation Cavitation (Ionization Nucleation)

Atoms surrounding us in everyday life are not very energetic, something on the order of 0.03 eV is an average energy on Earth. Though fast moving, molecules and atoms do not have sufficient energy to tear off each other's electrons. On the Sun, average kinetic energies of electrons, protons, and other charged particles in the plasma atmosphere approach 10,000 eV, and move with 1/10 the speed of light, especially in the magnetosphere. But in the outer reaches of space, even higher energy particles exist commonplace and stream through the Universe, some striking the Earth, and are collectively termed *cosmic rays* or *cosmic radiation*. Their composition has been measured recently, and cosmic rays are mostly hydrogen ions, with some helium, carbon, and oxygen ions too. Their energies are enormous, as high as 10^{14} eV, or 100 TeV. Cosmic ray energies are higher than energies of ions trapped in the magnetic field of the Earth. Cosmic rays stay around longer in the Galaxy than starlight, with starlight taking about 5,000 years to traverse the Milky Way, but trapped cosmic rays (weak galactic magenetic fields) take some 10^7 years to escape. The cosmic ray component of total radiation striking the Earth is 13%, and comprises most of the high energy tail of the spectrum.

Cosmic rays (charged particles, ions) passing through matter ionize the surrounding media in the process of slowing and stopping. Large amounts of their kinetic energy are deposited locally in the ionization process. Cavitation voids can be formed as charge separated surfaces emerge. As energy deposition and ionization rates increase, so do cavitation processes. If the tissue surrounding the cavitation voids is supersaturated, the seeds so formed can grow. The same holds for radioactive elements present in the body, such as U_{238} which decays by nuclear fission and releases many charged particle fragments into tissue and blood. In their gel experiments, Yount and Kunkle [46,68,89-91] examined nucleation rates from cosmic rays, including neutrons, and found the collective contribution to be less than 0.01 nucleation sites per gel sample (roughly 2,5 cm square or round dishes), well below experimental sensitivities and counting rates.

Cosmic ray energies are indeed huge, but the atmosphere shields us as effectively as a 10 ft layer of concrete. In the atmosphere, cosmic ray collisions produce high energy fragments in the GeV range, and some cosmic rays make it to the surface of the Earth, but overall, the intensity of radiation striking the surface from combined cosmic ray penetration is very small, on the order of 1/1000 the intensity of starlight. This is a very small number, and cavities produced by cosmic ray passage through the body are not only random, but small in number, on the order of a few a day.

Similarly, the fission of U_{238} in the body is expected to produce a cavity every couple of weeks. In both cases, it seems highly unlikely that either is an important source of micronuclei production, and therefore. not a strong contributing DCS factor.

Cavitation Hysteresis (Bubble Memory)

If a set of cavitation nuclei, denoted by number, κ_i, are observed in a sample following any process reducing vapor pressure locally below ambient pressure, then restoration of ambient pressure above vapor pressure to extinguish (remove) all nuclei is not a reversible process [3,16]. In fact, it's highly irreversible, in that, if the pressure is then restored to the initial value, the new set of cavitation nuclei, denoted κ_n, are different than the original distribution, κ_i. That is, $\kappa_n \neq \kappa_i$, akin to magnetic material hysteresis following a magnetization loop of materials to the same starting point. Cavitation processes do not conserve entropy, and hence, are highly irreversible. Cavitation materials retain a *cavitation memory*, likely due to structural changes following initial pressure reduction and cavitation void formation. The difference between the two quantities, κ_h, is called the *hysteresis index*,

$$\kappa_h = \kappa_i - \kappa_n$$

Cavitation hysteresis, without thinking about it much, has some bold implications for diving adaptation, reverse and repetitive profiles, tissue damage, denucleation, muscular movements during diving, and perfusion rates. If, for any forward or reverse profile,

$$\kappa_n \leq \kappa_i$$

forward or reverse profiles might be indicated. While, if

$$\kappa_n \geq \kappa_i$$

forward or reverse profiles might be contraindicated. To date, some experiments *in vitro* suggest the former, that is,

$$\kappa_n \leq \kappa_i$$

for successively decreasing pressure titrations. Such is a reason for forward profile diving admonitions, apart from obvious reductions in gas loadings under the same.

Homogeneous And Heterogeneous Nucleation

In studying holes, or weaknesses, in liquid structures, two dominant cavitation mechanisms emerge [1,4,5,13,18,29,56,68]:

1. *homogeneous nucleation* – thermal motions within the liquid form temporary microscopic voids that produce nuclei rupturing the voids, and subsequently growing into macroscopic bubbles;

2. *heterogenous nucleation* – major weaknesses develop at boundary layers between liquid and solid container walls, or between liquid and small particles suspended in the liquid, facilitating rupture and bubble growth.

The seemingly simple dichotomy above portends many very complex processes in the real world, not easily measured nor quantified in bubble science, and especially not in living systems.

Homogeneous nucleation along established classical lines (within the kinetic theory of liquids) only permits one kind of weakness, namely, the transitory voids that develop due to the thermal motion of liquid molecules. In real systems, of course, several other types of weaknesses and dislocations are possible. Nucleation may occur at the junction of a liquid and solid body. Kinetic theories have been developed quantifying such heterogeneous processes, while also quantifying the relative probabilities for homogeneous versus heterogeneous nucleation at the same site. Heterogeneous nucleation may also occur on very small, sub-micron size contaminants in the fluid, with the size of the contaminants

so small that differentiating homogeneous from heterogeneous nucleation is difficult to impossible in the laboratory.

Other weaknesses persist in liquids in the form of contaminant microbubbles, possibly present in crevices within boundaries, within suspended particles, or freely suspended in the liquid. These persistent weaknesses seem to resist dissolution completely. For instance, in water, microbubbles of air are virtually impossible to remove completely, perhaps due to interface contamination. While it's usually possible to remove such nuclei (denucleate) from small research samples, their presence persists in most engineering applications [1,58], and likely biomedical systems [56]. Much focus has centered on water systems, but not other liquids in general. Cosmic radiation is another component in nucleation processes. A collision between a high energy particle (any source, cosmic or otherwise) and a molecule of liquid can deposit enough energy locally to initiate nucleation. Such processes, of course, are fundamental to the operation of cloud and bubble chambers, and can be factors in promoting nucleation.

Simple homogeneous nucleation theory works very well for certain liquids, such as ether and n-hexane, in which nearly perfect denucleation has been demonstrated. For water at room temperatures, the opposite has been the case [22,26,28,33]. Homogeneous theory suggests a tensile strength for water near 1440 atm, corresponding to a critical radius of 10 $angstrom$ (10^{-3} μm) for vapor phases formed by random motion of water molecules. The highest tensile strength observed for water is 277 atm, while the highest supersaturation pressure sustained without cavitation is 270 atm in helium gas. Both are about 5 times below theoretical predictions, and this is generally taken as evidence that impurities ($motes$) remain present in even highly denucleated media, like water. Experimental attempts to seed liquids with solid impurities have not been very successful. For example, Bateman and Lang [4] tried charcoal, ferric oxide, and sodium bicarbonate with inconclusive results. Fischer [32] found that salt attracts nuclei into solution, but then dissolves completely so that nuclei are likely gaseous, and not solid. Polystyrene spheres [22] in the fractional micron size range, thought to resemble motes in water, were unsuccessful in nucleating gelatin. Cloud seeding [50,58] with iodine crystals has not produced rain in most circumstances. A consensus today is that smooth spheres of any size, hydrophobic or hydrophilic, only reduce the tensile strength of water by 25 % at most.

Studies of the formation of vapor voids in pure liquids date back to the pioneering work of Gibbs, with modern twists provided by Becker and Doring [5], and Zeldovich [92] in the middle 1900s. The dynamics of homogeneous nucleation are fairly simple. In a pure liquid, surface tension is the intermolecular force holding molecules together, thus preventing the formation of large holes in the liquid. Liquid ambient pressure, P, exterior to the bubble surface, is lesser than interior bubble pressure, Φ, by an amount,

$$\Phi - P = \frac{2\gamma}{r}$$

where γ is the surface tension, and r is the bubble radius. The concept of surface tension (better yet, surface energy) has been shown to be a very accurate concept even down to a few intermolecular distances by Skripov and others [13,65]. Perhaps such a simple description over a few molecular layers is surprising, but is nevertheless very useful.

The Gibbs free energy, G, for homogeneous nucleation processes is the sum of the energy deposited on the surface of the nucleus, $4\pi r^2\gamma$, plus the work done by the fluid to create the void, $4\pi r^3(p-p_b)/3$, with p_b the internal bubble pressure and p the external fluid pressure,

$$G = 4\pi r^2\gamma - \frac{4}{3}\pi r^3(p_b - p)$$

If a Laplace relationship is assumed across the bubble, we have,

$$p_b - p = \frac{2\gamma}{r}$$

and the usual expression for the free energy results. The work done by the fluid is not necessarily *ideal* dynamically, and other structures in, and around, the void may help or hinder the process. In such case, the Gibbs free energy is written,

$$G = 4\pi r^2 \gamma - \frac{4}{3}\pi r^3 \Psi$$

with Ψ a representation of the effective pressure difference across the bubble surface, $(p_b - p)$, for nonideal gas formation, external effects, bubble nonsphericity, and even heterogeneous impact on void formation. Some forms include,

$$\Psi = \beta(p_b - p)$$

with β a pressure difference multiplier,

$$\Psi = (p_b - p) + \delta$$

with δ an additive tissue compliance,

$$\Psi = \epsilon_b \ln \left[\frac{p_b}{p}\right]$$

for change in volumetric free energy in an isothermal phase expansion, where ϵ_b is the energy density in the bubble,

$$\Psi = \sum_{n=0}^{N} \alpha_n (p_b - p)^n$$

a virial expansion of the pressure difference, which can be fitted to data like an equation-of-state.

Homogeneous nucleation processes occur in single component systems, while heterogeneous nucleation processes involve more than one component. To describe nucleation, a heterogeneous model, ascribed to Plesset [58], containing the homogeneous case as a subset, has been useful in applications, as depicted in Figure 2. A solid hydrophobic sphere, of radius r_0, is surrounded by a concentric layer of vapor, out to a radius r. The instantaneous (Boltzmann) probability, dw, for the state depends on the difference in free energy, G, associated with the vapor phase,

$$dw = exp\ (-G/kT)\ dG$$

at temperature, T, for (Gibbs) free energy change, G,

$$G = \frac{4}{3}\pi r^2 \gamma_{lv} + \frac{4}{3}\pi r_0^2\ (\gamma_{vs} - \gamma_{ls})$$

and γ_{lv}, γ_{vs}, and γ_{ls} surface tensions associated with the liquid-vapor, vapor-solid, and liquid-solid interfaces. The homogeneous case corresponds to $r_0 = 0$, that is, no solid and only liquid-vapor nucleation. This particular form of the Gibbs energy is extensively used in Monte Carlo simulations of bubble excitation [2,21] and growth, homogeneous and heterogeneous.

Tensions, pulling parallel to their respective surfaces, at equilbrium have zero net component, as seen in Figure 2,

$$\gamma_{lv}\ cos\ \theta = \gamma_{vs} - \gamma_{ls}$$

with liquid-vapor contact angle, θ, measured through the liquid. Wetted (hydrophilic) solids exhibit acute contact angle, occurring when,

$$\gamma_{vs} - \gamma_{ls} > 0$$

so that the meniscus of the liquid phase is concave. In this case, the solid has greater adhesion for the liquid than the liquid has cohesion for itself, the free energy required to maintain the vapor phase is large (because the solid surface tension term is positive), and the probability of nucleation

is decreased by the solid impurity. For a nonwetting (hydrophobic) solid, the situation is reversed, that is, the contact angle is obtuse,

$$\gamma_{vs} - \gamma_{ls} < 0$$

the meniscus is convex, the solid has less adhesion for the liquid than the liquid has cohesion for itself, the free energy is reduced because the solid surface tension term is negative, and the probability of formation is increased. In the limiting case, $cos\ \theta = -1$, the free energy is given by,

$$G = \frac{4}{3}\pi\gamma_{lv}\ (r^2 - r_0^2)$$

which becomes small for cavity radius, r, near impurity radius, r_0.

In the above, a nucleation rate, j, is given by the Boltzmann energy partition function,

$$j = j_0\ exp\ (-G_b)$$

with G_b the Gibbs number,

$$G_b = \frac{G}{kT}$$

for normalization factor over free energy, j_0,

$$j_0 = \rho \left[\frac{2\gamma}{\pi m^3}\right]^{1/2}$$

with ρ the liquid density, and m the mass of the liquid molecule.

While theories of heterogeneous and homogeneous nucleation work well for a number of liquids, the application of the heterogeneous model to water with impurities is not able to reduce the tensile strength to observable values. Recall that the homogeneous theory of nucleation predicts a tensile strength of water near 1,400 atm, the heterogeneous theory, with a variety of solid impurities, drops the tensile strength down to 1,000 atm, and the measured value for water is approximately 270 atm. Yet, in any solution, gas nuclei can be deactivated (crushed) by application of large hydrostatic pressures. The process of *crushing* is also termed *denucleation*. When denucleated solutions are decompressed in supersaturated states, much higher degrees of supersaturation are requisite to induce bubble formation. In diving, denucleation has been suggested as a mechanism for acclimatization. If denucleation is size selective, that is, greater hydrostatic pressures crush smaller and smaller nuclei, and if number distributions of nuclei increase with decreasing radius (suggested by experiments), than a conservative deep dive, followed by sufficient surface interval, might in principle afford a margin of safety, by effectively crushing many nuclei and reducing the numbers of nuclei potentially excited into growth under compression-decompression. But this has not been proven in diving scenarios.

The mechanisms of nucleation in the body are obscure. Though nucleation most probably is the precursor to bubble growth, formation and persistence time scales, sites, and size distributions of nuclei remain open questions. Given the complexity and number of substances maintained in tissues and blood, heterogeneous nucleation would appear a probable mechanism. In that regard, the process of tribonucleation at tissue interfaces is a viable candidate for bubble seed production under even modest pressure reductions, certainly well below the 270 atm measured for water (watery tissue included).

Nucleation And Critical Droplets

As water cools to 0 ^oC, it freezes to ice. The molecules transform from the liquid phase to the solid, crystalline phase. At atmospheric pressure (1 atm), water will turn to vapor at 100 ^oC. Both of these phase transformations are abrupt. The molecule H_2O is water at 0.0001 ^oC and solid ice at -0.0001 ^oC. If salt or sugar are added to the water, slush will result over a range of temperatures. Abrupt phase transitions are called *first order transitions*. The transformation is abrupt as temperature changes, but happens more slowly if energy is added slowly. Water and ice coexist at the freezing temperature. An ice cube floating in water will maintain the freezing point throughout the cube until heat seeps in and melts the whole cube. Water when heated at the boiling point forms vapor bubbles. The energy required per unit mass to effect a phase transformation is the latent heat. Both ice cube in water and vapor bubbles in water have sharp boundaries separating them from water in the liquid phase. These boundaries are maintained by the surface tension, γ, or the free energy per unit surface area.

One can supercool or superheat within first order phase transitions. Very pure water, with no dust nor impurities within, in a very smooth container can be supercooled by many degrees, ΔT, below the freezing point and ice formation. Similarly, water vapor can be supercooled even above 110% humidity below the temperature of water droplet condensation. Supercooling and superheating within first order phase transformations can be effected because there exists a free energy barrier separating the two phases. Simply put, a large bubble of any new phase needs exist in any old phase before a new phase can grow. This is the essence of nucleation, providing a new phase site in the old phase to facilitate growth of the new phase. Small bubbles can't really grow the new phase well because the surface tension is large and the volume is small. Small bubbles pay a large cost in free energy per unit area for a small gain in volume.

Quantitatively, this is seen in the following way [21,28,51], and referring to Figure 3. The creation free energy, ΔG, for a droplet of radius, r, is the sum of the energy deposited in the surface of the droplet, $4\pi r^2\gamma$, plus the work done by the fluid in order to create the droplet, $4\pi r^3(p-p_b)/3$, with p the fluid pressure, and p_b the pressure inside the droplet,

$$\Delta G = 4\pi r^2\gamma - \frac{4}{3}\pi r^3(p_b - p)$$

At the critical radius, r_c,

$$(p_b - p)_c = \frac{2\gamma}{r_c}$$

and formation free energy, ΔG_c, becomes,

$$\Delta G_c = \frac{4}{3}\pi\gamma r_c^2 = \frac{16\pi}{3}\frac{\gamma^3}{(p_b-p)_c^2}$$

Denoting a specific formation energy, Δg_c, with m a mass, we have,

$$(p_b - p)_c = \Delta p_c = \rho\frac{\Delta G_c}{m} = \rho\Delta g_c$$

whereby, for entropy, s_c,

$$\Delta g_c = s_c\Delta T$$

In a phase transition,

$$s_c = \frac{l}{T_c}$$

with l the heat of transformation. Combining all,

$$\Delta G_c = \frac{16\pi\gamma^3 T_c^3}{3(\rho l \Delta T)^2}$$

Similarly, the critical radius, r_c, can be written, using the above,

$$r_c = \frac{2\gamma T_c}{\rho l \Delta T}$$

Plotting the free energy change, ΔG_c, versus radius, r_c, as depicted in Figure 3, a number of features are clear. The critical radius, r_c, gets bigger as supercooling or superheating temperature gradient, ΔT, decreases, and the barrier height, ΔG_c, also increases as the gradient decreases, actually as ΔT^2,

$$r_c \propto \frac{1}{\Delta T}$$

$$\Delta G_c \propto \frac{1}{\Delta T^2}$$

In Figure 3, $B = \Delta G_c$, and $\sigma = \gamma$.

The reason, then, that a container of water can be superheated or supercooled is the barrier, $B = \Delta G_c$, in Figure 3. To nucleate a droplet of new phase of radius, r_c, you must supply energy, B. The nucleation probability, n,

$$n = n_0 \; exp \; (-B/kT)$$

gives the relative probability of sitting atop the barrier. For small superheating, or supercooling, ΔT, the barrier, B, is large, and the nucleation probability, n, is very small. The nucleation probability can be so small, even though there is plenty of water and many places for droplets to form, that the probability of forming ice crystals or gas bubbles is negligible. Similar arguments apply to bubble and droplet formation in any media, including blood and tissue. Formation and stabilzation processes for bubbles are precipitous and bounded.

The above assume homogeneous nucleation. If dust particles, material defects, or flaws and gradations on the boundary surfaces are present, atoms in the unstable phase will use these particles or surfaces to bypass homogeneous nucleation, using impurities or surface flaws of characteristic dimensions, r_c. This process is then heterogeneous nucleation, as described.

Material Response

Under changes in ambient pressure (and temperature), bubbles will grow or contract, both due to dissolved gas diffusion and Boyle's law. An *ideal* change under Boyle's law is symbolically written, denoting initial and final pressures and volumes with subscripts, i and f, we have,

$$P_i V_i = P_f V_f$$

with bubble volume,

$$V = \frac{4}{3}\pi r^3$$

for r the bubble radius. The above supposes totally flexible (almost ideal elastomers) bubble films or skins on the inside, certainly not unrealistic for thin skin bubbles. Similarly, if the response to small incremental pressure changes of the bubble skins is a smooth and slowly varying function, the above is also true in low order. Obviously, the relationship reduces to,

$$P_i r_i^3 = P_f r_f^3$$

for an ideal radial response to pressure change.

But for real structured, molecular membranes, capable of offsetting constrictive surface tension, the response to Boyle's law is modified, and can be cast in terms of Boyle modifiers, ξ,

$$\xi_i P_i V_i = \xi_f P_f V_f$$

with ξ virial functions depending on P, V, and T. For thin and elastic bubble skins, $\xi = 1$. For all else, $\xi \neq 1$. For gels studied in the laboratory, as an instance, surfactant stabilized micronuclei do not behave like ideal gas seeds with thin elastic films. Instead under compression-decompression, their behavior is always less than ideal. That is to say, volume changes under compression or decompression are always less than computed by Boyle's law, similar to the response of a wetsuit, sponge, tissue bed, or lung membrane. The growth or contraction of seeds according to an equation-of-state (EOS) is more complex than Boyle's law [24,62], A *virial* expansion has for all P, T, V and mole fractions, n, for R the universal gas constant,

$$PV = nRT \sum_{i=0}^{N} \alpha_i \left[\frac{nT}{V}\right]^i$$

or, treating the virial expansion as a Boyle modifier, ξ,

$$\xi PV = nRT$$

across slowly varying data points and regions. Symbolically, the radius, r, can be cast,

$$r = \sum_{i=0}^{N} \beta_{i/3} \left[\frac{nRT}{P}\right]^{i/3}$$

or, again introducing Boyle modifiers, ζ,

$$\zeta r = \left[\frac{nRT}{P}\right]^{1/3}$$

for α and β standard virial constants. Obviously, the virial modifiers, ξ and ζ are the inverses of the virial sum expansions as power series. For small deviations from thin film bubble structures, both are close to one.

Observationally, though, the parameterization can take a different tack, following Yount [89-91]. In gel experiments, the EOS is replaced by two regions, the permeable (simple gas diffusion across the bubble interface) and impermeable (rather restricted gas diffusion across the bubble interface). In the permeable region, seeds act like thin film bubbles for gas transfer. In the impermeable region, seeds might be likened to beebees. An EOS of course recovers this response in both limits. Accordingly, just in gels, the corresponding change in critical radius, r, following compression, $(P - P_i)$, in the *permeable* region, satisfies a relationship,

$$(P - P_i) = 2(\gamma_c - \gamma)\left[\frac{1}{r} - \frac{1}{r_i}\right]$$

with γ_c maximum compressional strength of the surfactant skin, γ the surface tension, and r_i the critical radius at P_i. When P exceeds the structure breakpoint, P_c, an equation for the *impermeable* region must be used. For crushing pressure differential, $P - P_c$, the gel model requires,

$$P - P_c = 2(\gamma_c - \gamma)\left[\frac{1}{r} - \frac{1}{r_c}\right] + P_c + 2P_i + P_i\left[\frac{r_c}{r}\right]^3$$

where,

$$r_c = \left[\frac{P_c - P_i}{2(\gamma_c - \gamma)} + \frac{1}{r_i} \right]^{-1}$$

is the radius of the critical nucleus at the onset of impermeability, obtained by replacing P and r with P_c and r_c above. Allowed tissue supersaturation, $\Delta\Pi$, is given by,

$$\Delta\Pi = 2 \ \frac{\gamma}{\gamma_c r}(\gamma_c - \gamma)$$

with, in the permeable region,

$$r = \left[\frac{(P - P_i)}{2(\gamma_c - \gamma)} + \frac{1}{r_i} \right]^{-1}$$

and, in the impermeable region,

$$r^3 - 2(\gamma_c - \gamma)r^2 - \frac{P_i}{\zeta} r_c^3 = 0$$

for,

$$\zeta = P - 2P_c + 2P_i + \frac{2(\gamma_c - \gamma)}{r_c}$$

So, allowed supersaturation is a function of three parameters, γ, γ_c, and r_i. They can be fitted to exposures and lab data. But Boyle expansion or contraction needs be applied ad hoc to the excited seeds. Additionally, nuclei generate over times scales, ω, such that,

$$r = r_0 + [1 - \exp \ (-\omega t)](r_i - r_0)$$

with r_0. the critical radius at initial time ($t = 0$). The fourth parameter, ω^{-1}, is on the order of of minutes to hours, but was never really codified in the Yount gel experiments. In the blood and tissue of divers, regeneration of seeds links perhaps to exercise and activity, rather than to persistence over longer time scales, but the exact situation remains unclear [36,68,71].

Blood And Tissue Bubbles

For watery blood (mostly water), densities are nominal,

$$1.00 \leq \rho \leq 1.15 \ g/cm^3$$

while surface tension depends upon lipid or aqueous preponderance in tissues and blood,

$$15 \leq \gamma \leq 80 \ dyne/cm$$

with smaller values for lipids, and larger values for watery tissue. The ram coefficient varies,

$$0.5 \leq \omega \leq 2.0$$

while the viscosity ranges,

$$0.0100 \leq \eta \leq 0.0400 \ dyne \ sec/cm^2$$

Considering blood flow speeds in the systemic circulation of the body, less than 25 cm/sec (vena cava), flow regimes for bubbles are mostly laminar, with low Reynolds numbers. Complicated patterns in and around heart valves are not laminar, but still low speed. Said another way, bubbles in blood flows can be treated mostly with Stokes parameterization (and simplicity).

Bubble Flow Regimes

Treating bubbles in the circulatory system as semi-solid spheres of radius a, we can estimate the onset of turbulent bubble flow as a function of bubble size and blood flow rate (varying considerably across the body proper). The smaller the bubble, of course, the more persistent is the bubble, and the solid sphere approximation gets better. Taking 0.50 as rough cutoff Reynolds number for laminar bubble flow in the body, we have for corresponding cutoff bubble radius, a,

$$Re = \frac{\rho u a}{2\eta} \leq 0.50$$

so that,

$$a \leq \frac{2 \times 0.50\eta}{\rho u} \leq 0.0004\ cm$$

for nominal density and viscosity, and maximum blood flow. Roughly, bubbles smaller than 4 μm flow smoothly. At slower blood speeds, larger bubbles are accommodated, as well as at larger viscosities. Interestingly, intercellular cell separations range in the 10 - 20 μm range, likely permitting such flow regime. Flow speeds 5 times slower suggest laminar bubbles on the order of 20 μm here, impinging boundaries at the upper end of separations.

Bubble Flow Distortion

Bubbles are pliable and distensible, deviating from sphericity under increasing stress and flow pressure. Experiment and theory underscore gradual change from spherical bubbles to oblate bubbles as relative flow speeds between bubble and fluid media increase in magnitude. Beyond extreme bubble distortion, bubble fracture takes place. Let's take a look at bubble distortion first.

For a moving bubble in a fluid, solving the two phase equations numerically, and introducing Eotvos number, Eo, Morton, Mo, Weber number, We, with Reynolds number, Re, and drag coefficient, κ,

$$Eo = \frac{\rho d^2 g}{\gamma}$$

$$Mo = \frac{g\kappa^4 \rho^3}{\gamma^3}$$

$$We = \frac{\rho^2 w^2 d}{\gamma}$$

$$Re = \frac{wd}{\gamma}$$

$$\kappa = \frac{4gd}{3w^2}$$

for, w, the bubble velocity, d, the bubble diameter,

$$d = \left[\frac{6V}{\pi}\right]^{1/3}$$

and V the bubble volume, permits a rough catergorization of bubble distortion as seen in Figure 4. For water and blood at 20 ^oC, we have $Mo = 3 \times 10^{-11}$ in dimensionless units, with all other quantities nominally as before. The Eotvos number represents the ratio of gravitational to capillary forces, the Morton number tags fluid properties only, the Weber number scales inertial to capillary forces, the Reynolds number tags inertial and viscous force ratios, while the drag coefficient contrasts gravitational and inertial force ratios. Relative shapes of bubbles are indicated by graph icons. The diagonal, curved line through the distortion graph tags the transition region for spherical to nonspherical bubble shapes, while the ascending asymptotes represent constant Morton number, Mo.

For 1 *micron* bubbles moving at 25 cm/sec, we have $Eo = 2 \times 10^{-6}$, and $Re = 0.50$ roughly, so that much deviation from sphericity is unlikely in the media. For 1,000 *micron* bubbles moving at the same rate, we get $Eo = 2$, and $Re = 50$, putting us into the distortion regime of flow dynamics. In the former case, the surface tension and small bubble size make it relatively impervious to flow distortion, while in the latter case, the large bubble size accommodates considerable flow distortion.

Bubble Flow Fracture

Similar to flow analysis, some ball park estimates on blood bubble breakup can be made. Surface tension, γ, of course varies across lipid and aqueous tissues, by some factor of 5 to 6, perhaps even more according to high pressure studies of thin film bubble permeabilities. From the foregoing, we have the fracture cutoff, a, in watery flows,

$$a \geq \frac{4\gamma}{\omega \rho g u^2} \geq 0.0068 \ cm$$

and, in lipid flows,

$$a \geq 0.0408 \ cm$$

which are fairly large fracture radii. Below blood speeds of 25 cm/sec, the fracture radii increase considerably, obviously inversely as the flow speed squared. It would thus appear from these back of the envelope estimates that flow fracture is unlikely for 100 μm bubbles, and smaller.

Bubble Shock Fracture

Rapidly applying high pressure to a liquid will fracture bubbles and seeds. Tapping a pressurized container of liquid will often eliminate bubbles (denucleation) when pressure is released. This is often done with soft drinks. Such procedures generate pressure waves in the liquid which can fracture seeds. Treating the bubbles as an ideal gas, and denoting the pressure differential across the shock wave, $P_f - P_i$, with f and i denoting final and initial shock pressures, we have from the Rankine-Hugoniot jump equations [25], with c_P and c_V specific heats at constant pressure, P, and constant volume, V, M the Mach number (shock speed divided by sound speed in the media), and $M > 1$,

$$P_f - P_i = P_i \left[\frac{2c_P/c_V}{c_P/c_V + 1}(M^2 - 1) \right] \geq \frac{2\gamma}{r}$$

as a simple mechanical estimate for a pressure wave to exceed bubble surface tension. Taking $c_P/c_V = 5/3$ for an ideal gas, we see,

$$P_i \geq \left[\frac{8\gamma}{5r(M^2 - 1)} \right]$$

yielding a threshold pressure, P_i, for fracturing a bubble of radius, r. Turning the equation around, the threshold radius, r, for fracture under shock passage with initial pressure, P_i, is given by,

$$r \geq \left[\frac{8\gamma}{5P_i(M^2 - 1)} \right]$$

If the ratio of shock speed to sound speed, M, is small, then large pressures, P_i, are necessary for fracture. Or, only large bubbles are fractured when the Mach number, M, is small.

Bubble Buoyancy

Gas bubbles in fluids will usually float, but very small bubbles with high density gas trapped inside can sink. In blood and tissues, a cutoff radius for floating and sinking bubbles can be estimated in an approximate sense, treating viscosity as a low order effect, or in the case that the bubble velocity (rising or sinking) is small. For watery tissue and blood, with nominal density, $\rho = 1.15 \ g/cm^3$, bubbles of density ρ' will rise provided,

$$\rho' < 1.15 \ g/cm^3$$

or, denoting the mass of trapped gas in the bubble, m',

$$m' < \frac{4 \times 1.15}{3} \pi a^3 \ g = 4.82 a^3 \ g$$

A bubble will sink, alternatively, for the opposite case,

$$m' > \frac{4 \times 1.15}{3} \pi a^3 \ g = 4.82 a^3 \ g$$

Table 1 lists the cutoff radii, a, for bubble 1s ranging from 1 g to 1 ng, plus corresponding surface tension pressure at the cutoff radii.

Table 1. Bubble Cutoff Radii And Surface Tension Pressure

a (cm)	m' (g)	$2\gamma/a$ $(dynes/cm^2)$
0.5920	10^0	28.7
0.2748	10^{-1}	61.8
0.1275	10^{-2}	133.2
0.0592	10^{-3}	286.9
0.0275	10^{-4}	618.3
0.0128	10^{-5}	1332.1
0.0059	10^{-6}	2869.7
0.0027	10^{-7}	6182.4
0.0013	10^{-8}	13319.5
0.0006	10^{-9}	28695.6
0.0003	10^{-10}	61821.8

Bubble masses in the body are thought to roughly range,

$$10 \leq m' \leq 0.10 \ ng$$

where, 1 $ng = 10^{-9}$ g.

Putting the above together, a few comments about body bubbles seem clear. Bubbles with radii larger than listed, for given mass, will rise, while those with radii smaller than listed, will sink in blood and watery tissue. Recall that 1 $\mu m = 10^{-4}$ cm, so bubbles in the 1 to 15 $micron$ range exhibit enormous surface tension in the body, with some floating up to the capillary boundaries and some sinking. Some will tumble along circulatory boundaries, while others will be be destroyed by the contact. Others, near hydrodynamic and static equilibrium, will be carried along by the flow. New bubbles, created by cavitation, nucleation, and crevitation, may dump into the blood flow, or remain trapped at birth sites. Large bubbles in the blood flow may fracture spontaneously, or possibly be eliminated by the filter systems of the lung and pulmonary circulation. Some (very small) may survive all destruction mechanisms, and pass back out into the arterial and systemic circulation. The scenarios are complex, and virtually intractable. As pressure changes, bubbles support gradients for gas transport across thin film boundaries, changing bubble sizes and properties along the way. Even without pressure changes, constrictive surface tension will tend to collapse bubbles with radii less than critical values.

Blood And Tissue Cavitation

As seen for water, the incipient cavitation index, κ_i, is of order of 1.0, at room temperature and sea level pressure (1 atm). This offers a good baseline for spontaneous cavitation estimates in flowing blood, laminar and turbulent. Taking a maximum blood flow rate of 30 cm/sec, and treating

blood as water (density), the cavitation index at sea level can be first estimated. Taking water vapor pressure at body temperature to be as high as 0.10 atm, we see easily,

$$\kappa = 2024.50$$

while at 18,000 ft elevation, with pressure roughly 0.5 atm, we find,

$$\kappa = 900.66$$

Both are far above the incipient value, and laminar blood flow cavitation is highly unlikely. Blood flows with a rotational component, possibly with small vortices in and around heart valves and bending constrictions, support higher cavitation numbers, but not below the incipient index. If vortex pressure reduction is even 25% of ambient pressure, all other factors the same, the cavitation index is roughly at sea level,

$$\kappa = 337.75$$

and at 18,000 ft elevation,

$$\kappa = 56.29$$

Both cavitation numbers are still far above the incipient value, and rotational blood flow cavitation remains highly unlikely. Vortex pressure would need be reduced to roughly 0.1005 atm to drop the cavitation index near unity, and below. Suffice to say that flow cavitation in the blood requires ambient pressure reductions near vapor pressure for the very low blood speeds in the body. Even if blood densities are doubled, cavitation numbers are only halved, and cavitation in highly lipid blood flows remains unlikely. Tissue cavitation is another question, with a more likely probability.

In tissues, cavitation seems likely as tissue surfaces rub together. Tribonucleation might manifest itself in a number of sites in biological systems. Numerous sites exist where surfaces may contact each other and rub across one another. Articulating joints are a possibility, whereby synovial fluid may display a high enough viscosity to mimic experiments in the laboratory, as suggested by Ikels. Small circulatory vessels may collapse and expand in response to muscle movement, as well as ligatures and tendons connected to bone joints. Negative tensions, τ, as low as 0.10 atm support bubble formation between plates submersed in oil and separated with velocity as low as 0.7 cm/sec, The higher the separation speed, the greater the number of bubbles formed in experiments. We can use these results to estimate muscle separation speed, u, or contact ratio, χ, that is, the ratio of muscle surface area, A, to separation volume, V,

$$\chi = \frac{A}{V}$$

for tribonucleation in body tissue interfaces. First, we have,

$$\tau \leq \eta u \chi$$

or,

$$u \geq \frac{\tau}{\eta \chi}$$

Taking tissue (fluid) viscosity, $\eta = 0.02$ $dyne\ sec/cm^2$, a value between water and glycerol, $\chi = 2 \times 10^7\ cm^{-1}$ from experiments by Campbell [20], and $\tau = 0.10\ atm$, we estimate (minimal) muscle separation speed, u,

$$u \geq 0.25\ cm/sec$$

This targets a speed range of muscle motion with small velocity for producing tribonuclei according to adhesion dynamics. Rubbing tissues are certainly capable of generating negative tensions in the atm range, as suggested in kinesiological studies [43]. The contact ratio, χ, is a crucial controlling factor in tribonucleation. It can vary rapidly for different surface separations in fluids, that is,

small changes in surface separations induce large changes in the ratio. Obviously, χ is unknown for tribonucleation in the body, though η and u can be resaonably estimated.

If the fluid media supports gas tension, p, bubble formation is enhanced, and a Laplacian relationship is assumed,

$$p - \tau = \frac{2\gamma}{r}$$

with the tension reduced by the negative void pressure, τ. Bubble sizes vary inversely as the pressure differences, as verified by many investigators [1,4,5,20,29,50,90].

Rayleigh-Plesset Bubble Equation

A detailed picture of a bubble in a moving fluid is afforded by the Rayleigh-Plesset equation [29,58,63]. It is a useful tool for analyzing cavitation damage and bubble collapse in many flow regimes, and the dynamics are briefly recounted here. No discussion of bubble mechanics would likely be complete without it.

A first analysis of problems in cavitation and bubble damage was undertaken by Rayleigh in 1917, detailing the collapse of a cavity in a large mass of fluid, as well as related behavior of a gas void under isothermal compression. His interest in the problem relates directly to concerns of the Royal Navy with propellor damage, for which Rayleigh was commisioned to investigate the cause. Rayleigh, neglecting liquid viscosity and surface tension under the assumption of an incompressible fluid, showed from the momentum fluid equations that the bubble wall, r, obeyed the relationship, with ρ the fluid density,

$$\rho r \frac{\partial^2 r}{\partial t^2} + \rho \frac{3}{2} \left[\frac{\partial r}{\partial t} \right]^2 = p_r - p$$

for p the fluid pressure away from the bubble, and p_r the fluid pressure at the bubble surface. From the Bernoulli relationship, the pressure in the liquid, p_r, taking into account liquid viscosity, ν, and surface tension, γ, was suggested by Plesset,

$$p_r = p_b - \frac{2\gamma}{r} - \frac{4\nu}{r} \frac{\partial r}{\partial t}$$

The resulting Rayleigh-Plesset equation takes the standard form,

$$\rho r \frac{\partial^2 r}{\partial t^2} + \rho \frac{3}{2} \left[\frac{\partial r}{\partial t} \right]^2 = p_b - p - \frac{2\gamma}{r} - \frac{4\nu}{r} \frac{\partial r}{\partial t}$$

Both bubble pressure and fluid pressure are functions of time, that is,

$$p_b = p_b(t)$$

$$p = p(t)$$

and the usual critical radius, r_c, is,

$$r_c = \frac{2\gamma}{p_b - p}$$

as before.

The equation has some interesting features. Taking just the homogeneous part,

$$\rho r \frac{\partial^2 r}{\partial t^2} + \rho \frac{3}{2} \left[\frac{\partial r}{\partial t} \right]^2 = 0$$

with boundary conditions, $r = r_0$ at $t = 0$, and $r = 0$, at $t = t_c$, we find,

$$r = r_0 \left[\frac{t_c - t}{t_c} \right]^{2/5}$$

representing a collapsing bubble with wall velocity singularity at $t = t_c$, that is,

$$\frac{\partial r}{\partial t} = -\frac{2}{5}\left[\frac{t_c}{t_c - t}\right]^{3/5}$$

which approaches infinity at t_c. The singularity itself predicts cavitation damage via sonic waves at collapse (*sonocollapse*). The pressure waves produced by collapse are strong enough to damage material surfaces (like propellors), and are strong shock waves. If a sinusoidal pressure variation is imposed on the fluid,

$$p = p_0[1 + \epsilon\ cos\ (\omega t)]$$

with p_0 average ambient pressure, and ϵ a small pressure perturbation, the bubble surface will oscillate at natural resonant frequences, emitting sound while oscillating. Neglecting higher order harmonics in the oscillation spectrum (higher frequency oscillations damp in time), the lowest ($n = 0$) eigenfrequency is given by,

$$\omega_0^2 = 5\frac{p_0}{\rho r_c^2} - \frac{2\gamma}{\rho r_c^3}$$

Underwater, the sound emissions crackle like hail on concrete. If the driving amplitude, p_0, is high enough (20% to 40% above ambient pressure), on Rayleigh collapse, the bubble emits a short pulse of light (*sonoluminescence*). Drive frequencies in the *kilohertz* regime are necessary to pump the bubble. On compression, the gas in the bubble heats up rapidly, and partially ionizes at temperatures near 14,000 ^oK. On collapse with recombination, thermal brehmstrahlung is released as characteristic light emission.

The (famous) evolution of two gas bubbles below a free surface is also treated within the framework of the Rayleigh-Plesset equation, and we sketch details briefly for the interested reader. The system configuration is shown in Figure 5 (upper part). Assume both bubbles are simultaneously initiated as high pressure spherical ensembles, both at the same distance, h, from the free surface. The exclusion distance between their centers is denoted, $2d$. The pressure inside each bubble is the sum of the vapor pressure from the surrounding liquid plus the pressure of the noncondensing gas. Assuming the noncondensing gas is ideal, and its expansion and compression are adiabatic, the gas pressure inside the bubble, p_b, can be expressed in terms of its volume, V, as,

$$p_b = p + p_o\left[\frac{V_o}{V}\right]^{\kappa}$$

with $\kappa = c_P/c_V = 5/3$, V_o the volume of the bubble at noncondensing gas pressure, p_o, and p the vapor contribution. The fluid is assumed inviscid, incompressible, and irrotational, with velocity potential, ϕ,

$$\nabla^2\phi = 0$$

so that the fluid velocity, $\mathbf{u}$, obtains from the velocity potential,

$$\mathbf{u} = \nabla\phi$$

The potential, ϕ, derives from a surface Green function, G, integrated across the surface, S, within solid angles, Ω, subtending fluid points at distance, r, from the boundary surface,

$$\phi = \int_\Omega [G\nabla\phi - \phi\nabla G] \cdot d\mathbf{S}$$

for,

$$G = \frac{1}{4\pi r}$$

and r the distance from the boundary to the fluid point in question. The bubble surfaces are governed by kinematic and dynamic boundary conditions, namely, in dimensionless scaled distance and pressure units,

$$\frac{d\mathbf{r}}{dt} = \nabla\phi$$

outside the bubbles, and,

$$\frac{d\phi}{dt} = 1 + \frac{1}{2}(\nabla\phi)^2 + \delta^2(z-\zeta) - \epsilon\left[\frac{V_o}{V}\right]^{\kappa}$$

inside the bubbles, for $\delta^2 = \rho g R_c/(p_b - p)$, $\epsilon = p_o/(p_b - p)$, $\zeta = h/R_c$, R_c the critical bubble radius, and,

$$\frac{d\phi}{dt} = \frac{1}{2}(\nabla\phi)^2 - \delta^2 z$$

on the free surface. If buoyancy and boundary effects on bubbles are neglected, the Rayleigh-Plesset equation reduces to the Rayleigh expression in radial form, closing the bubble set of equations,

$$R\frac{d^2R}{dt^2} + \frac{3}{2}\left[\frac{dR}{dt}\right]^3 = \epsilon\left[\frac{R_0}{R}\right]^{3\kappa} - 1$$

in dimensionless units also.

The system of equations is only amenable to numerical solution, supercomputers being requisite for 3D resolution on the types meshes shown in the bottom half of Figure 5. Rayleigh never had such computing power on his desk, and his accomplishments in bubble dynamics, cavitation, and material damage are truly remarkable. Even mesh generation in Figure 5 requires supercomputing power, tetrahedral volume elements laced strategically to smoothly contour all surfaces in 3D.

Micronuclei Distributions And Lifetimes

Most questions of seed distributions, lifetimes, persistence, and origins in the body are unanswered today [4,18,30,31,36,39,41,46,55,69,72,74,77-79]. And while we have yet to measure microbubble distributions and lifetimes in the body, we can gain some insight from laboratory measurements and statistical mechanics. Microbubbles typically exhibit size distributions that decrease exponentially in radius, r. Holography measurements of cavitation nuclei in water tunnels suggest, fitting data from Mulhearn [50],

$$N = N_0\ exp\ (-\beta r)$$

with,

$$N_0 = 1.017 \times 10^{12}\ m^{-3}$$

$$\beta = 0.0512\ \mu m^{-1}$$

The Yount experiments in gels also display exponential dependences in cavitation radii,

$$N = N_0\ exp\ (-r/\alpha)$$

with,

$$N_0 = 662.5\ ml^{-1}$$

$$\alpha = 0.0237\ \mu m$$

Both MRI and Doppler laser measurements of water and ice droplets [45] in the atmosphere underline exponential decrease in number density as droplet diameter increases. Ice and water droplets in clouds typically range, $2\ \mu m \leq r \leq 100\ \mu m$. Dust and pollutants [51] are also exponentially distributed,

potentially serving as heterogeneous nucleation sites. It might be a surprise if micronuclei in the body were not exponentially distributed in number density versus size.

The lifetimes of cavitation voids are not known, nor measured, in the body. The radial growth equations provide a framework for estimation using nominal blood and tissue constants. Consider first the mass transfer equation,

$$\frac{\partial r}{\partial t} = \frac{DS}{r}\left[\Pi - P - \frac{2\gamma}{r}\right]$$

with all quantities as before, that is, r bubble radius, D diffusivity, S solubility, γ surface tension, P ambient pressure, and Π total gas tension. The time to collapse, τ, can be obtained by integrating over time and radius, taking initial bubble radius, r_i,

$$\tau = \int_0^\tau dt = \int_{r_i}^0 \left[\frac{r}{DS}\right]\left[\frac{1}{\Pi - P - 2\gamma/r}\right] dr = \left[\frac{\Delta p r_i(4\gamma + \Delta p r_i) - 8\gamma^2 \ln\ (2\gamma/2\gamma - \Delta p r_i)}{2DS\Delta p^3}\right]$$

with,

$$\Delta p = P - \Pi$$

If surface tension is suppressed, we get,

$$\tau = \frac{r_i^2}{2DS\Delta p}$$

In both cases, small tension gradients, Δp, and small transport coefficients, DS, lead to long collapse times, and vice-versa. Large bubbles take a longer time to dissolve than small bubbles. Taking nominal transport coefficient for nitrogen, $DS = 56.9 \times 10^{-6} \mu m^2/sec\ fsw$, and initial bubble radius, $r_i = 10.0\ \mu m$, for $\Delta p = 3.0\ fsw$, and $\gamma = 40\ dynes/cm$, we find,

$$\tau = 0.25\ sec$$

In the Rayleigh-Plesset picture, the radial growth equation takes the earlier form, neglecting viscosity,

$$\left[\frac{\partial r}{\partial t}\right]^2 = \frac{2(\Pi - P)}{3\rho}\left[\frac{r_i^3}{r^3} - 1\right] + \frac{2\gamma}{\rho r}\left[\frac{r_i^2}{r^2} - 1\right]$$

so that the collapse time by diffusion only is,

$$\tau = \int_0^\tau dt = \left[\frac{3\rho}{2(\Pi - P)}\right]^{1/2} \int_{r_i}^0 \left[\frac{r_i^3}{r^3} - 1\right]^{-1/2} dr = r_i\ \frac{\Gamma(5/6)}{\Gamma(1/3)}\left[\frac{3\pi\rho}{2\Delta p}\right]^{1/2}$$

with,

$$\Gamma(5/6) = 1.128$$

$$\Gamma(1/3) = 2.679$$

Suppressing the diffusion term in the growth equation, there similarly obtains,

$$\tau = \int_0^\tau dt = \left[\frac{\rho}{2\gamma}\right]^{1/2} \int_{r_i}^0 r^{1/2}\left[\frac{r_i^2}{r^2} - 1\right]^{-1/2} dr = r_i\ \frac{\Gamma(-3/4)}{\Gamma(-1/4)}\left[\frac{\pi\rho r_i}{4\gamma}\right]^{1/2}$$

with,

$$\Gamma(-3/4) = -4.834$$

$$\Gamma(-1/4) = -4.062$$

Collapse time in the Rayleigh-Plesset picture is linear in initial bubble radius, r_i, and inversely proportional to the square root of the tension gradient, Δp, or the surface tension, γ. Taking all quantities as previously, with density, $\rho = 1.15\ g/cm^3$, we find with surface tension suppressed,

$$\tau = 2.91 \times 10^{-3}\ sec$$

and, for the diffusion term term suppressed with only the surface tension term contributing,

$$\tau = 2.52 \times 10^{-6}\ sec$$

Dissolution times above range,

$$10^{-6}\ sec \leq \tau \leq 10^{-1}\ sec$$

In the Yount model of persistent nuclei, within the permeable gas transfer region, seed nuclei lifetimes, τ, range,

$$10^{-6}\ sec \leq \tau \leq 10^{-2}\ sec$$

The collapse rate increases with both γ and Δp, and inversely with r_i. Small bubbles collapse more rapidly than large bubbles, with large bubble collapse driven most by outgassing diffusion gradients and small bubble collapse driven most by constrictive surface tension. Between these extrema, both diffusion and surface tension play a role. In any media, if stabilizing material attaches to micronuclei, the effective surface tension can be reduced considerably, and bubble collapse arrested temporarily, that is, as $\gamma \rightarrow 0$ as a limit point. For small bubbles, this seems more plausible than for large bubbles because smaller amounts of material need adhere. For large bubbles, bubble collapse is not aided by surface tension as much as for small bubbles, with outgassing gradients taking longer to dissolve large bubbles than small ones. In both cases, collapse times are likely to lengthen over the short times estimated above. Additionally, external influences on the bubble, like crevices and surface discontinuities, may prevent bubble growth or collapse. All this adds to the bubble dilemmas faced by hydrodynamicists and modelers.

Computational Algorithms

Bubble models address the coupled issues of gas uptake and elimination, bubbles, and pressure changes in different computational approaches. Application of a computational model to staging divers and aviators is often called a diving algorithm. Consider the computational model and staging regimen for some published algorithms, namely, diffusion, perfusion (2), thermodynamic, varying permeability, reduced gradient bubble, modified gradient phase, tissue bubble diffusion, and linear-exponential phase algorithms. Dissolved gas models are listed first, followed by dual phase and bubble models thereafter.

Dissolved gas diving algorithms historically trace back to the original Haldane experiments in the early 1900s. They are still around today, in tables, meters, and diving software. That is changing, however, as modern divers go deeper, stay longer, decompress, and use mixed gases.

Diffusion Model (DM)

The DM dates back to the time of Haldane, representing an alternative [37,60,74] to bulk multitissue transfer equations (discussed next) with more structure imbedded. Exchange of inert gas, controlled by diffusion across regions of varying concentration, is also driven by the local gradient. Denoting the arterial blood tension, p_a, and instantaneous tissue tension, p, the gas diffusion equation takes the form in one dimensional planar geometry,

$$D\frac{\partial^2 p}{\partial x^2} = \frac{\partial p}{\partial t}$$

with D a single diffusion coefficient appropriate to the media. Using standard techniques of separation of variables, with ω^2 the separation constant (eigenvalue), the solution is written,

$$p - p_a = (p_i - p_a) \sum_{n=1}^{\infty} W_n \ sin \ (\omega_n x) \ exp \ (-\omega_n^2 D t)$$

assuming at the left tissue boundary, $x = 0$, we have $p = p_a$, and with W_n a set of constants obtained from the initial condition. First, requiring $p = p_a$ at the right tissue boundary, $x = l$, yields,

$$\omega_n = \frac{n\pi}{l}$$

for all n. Then, taking $p = p_i$ at $t = 0$, multiplying both sides of the diffusion solution by $sin \ (\omega_m x)$, integrating over the tissue zone, l, and collecting terms gives,

$$W_{2n} = 0$$

$$W_{2n-1} = \frac{4}{(2n-1)\pi}$$

Averaging the solution over the tissue domain eliminates spatial dependence, that is $sin \ (\omega_n x)$, from the solution, giving a bulk response,

$$p - p_a = (p_i - p_a) \sum_{n=1}^{\infty} \frac{8}{(2n-1)^2 \pi^2} exp \ (-\omega_{2n-1}^2 D t).$$

The expansion resembles a weighted sum over $effective$ tissue compartments with time constants, $\omega_{2n-1}^2 D$, determined by diffusivity and boundary conditions. Unlike the perfusion case, the diffusion solution, consisting of a sum of exponentials in time, cannot be formally inverted to yield time remaining, time at a stop, nor time before flying. Such information can only be obtained by solving the equation numerically, that is, with computer or hand calculator for given M_0, ΔM, a, and b. Diffusion models fit the time constant, κ,

$$\kappa = \frac{\pi^2 D}{l^2}$$

to exposure data, with a typical value from the Royal Navy [38-40,60] given by,

$$\kappa = 0.007928 \ min^{-1}.$$

The diffusion coefficient, D, however, for the above time constant, κ, above is of order $10^{-10} \ cm^2/sec$, five orders of magnitude slower than the aqueous tissue value, $10^{-5} \ cm^2/sec$, roughly. As such, it tracks morely closely the perfusion limited, multitissue model linked originally to Haldane [15]. The approach is aptly single tissue, with equivalent tissue halftime, τ_D,

$$\tau_D = \frac{0.693}{\kappa} = 87.5 \ min$$

close to the US Navy 120 minute compartment used to control saturation, decompression, and repetitive diving. Corresponding critical tensions in the bulk model, take the form,

$$M = \frac{709 \ P}{P + 404}$$

falling somewhere between fixed gradient and multitissue values. At the surface, $M = 53 \ fsw$, while at 200 fsw, $M = 259 \ fsw$. A critical gradient, G, satisfies,

$$G = \frac{M}{0.79} - P = \frac{P \ (493 - P)}{(P + 404)}.$$

The staging regimen is,

$$p \leq M$$

Salient features of the bulk diffusion model can be gleaned from extension of the above slab model in the limit of thick tissue region, that is, $l \rightarrow \infty$. Replacing the summation over n with an integral as $l \rightarrow \infty$, we find

$$p - p_a = (p_i - p_a)\ \bar{erf}\ [l/(4Dt)^{1/2}]$$

with $\bar{erf}$ the average value of the $error - function$ over l, having the limiting form,

$$\bar{erf}\ [l/(4Dt)^{1/2}] = 1 - (4Dt)^{1/2} l \pi^{1/2}$$

for short times, and

$$\bar{erf}\ [l/(4Dt)^{1/2}] = \frac{l}{(4\pi Dt)^{1/2}}$$

for long times. The former case recovers the Hempleman [38] square root law for no decompression time versus depth. A variant of the model couples different *compartments* in series or parallel, assigning different properties to the compartments, and imposing flux continuity at the boundaries. Such allows for tissue-blood interface differences, and is called the n-compartment model [6,40,53,54], with n the number of different tissue cells. It's been a mainstay in DCIEM [10,53,54] diving applications.

The DM has seen extensive testing, correlation, and use by the Royal Navy. It forms the bases of British technical and recreational dive tables, as well as other segments of the Europoean diving community at large. It was the first model employed in a mechanical analog decompression meter in the early 1970s.

Multitissue Model (MTM)

The multitissue model (MTM) was originally proposed by Haldane [15], with modern correlations and tunings [6,12,37,44,61,75,85] dating back to the 1950s. Exchange of inert gas, controlled by blood flow rates across regions of varying concentration, is driven by the gas gradient, that is, the difference between the arterial blood tension, p_a, and the instantaneous tissue tension, p. This behavior is modeled in time, t, by classes of exponential response functions, bounded by p_a and the initial value of p, denoted p_i. These multitissue functions satisfy a differential perfusion rate equation,

$$\frac{\partial p}{\partial t} = -\lambda (p - p_a)$$

and take the form, tracking both dissolved gas buildup and elimination symmetrically,

$$p - p_a = (p_i - p_a)\ exp\ (-\lambda\ t)$$

$$\lambda = \frac{0.693}{\tau}$$

with perfusion constant, λ, linked to tissue halftime, τ. Compartments with 1, 2.5, 5, 10, 20, 40, 80, 120, 180, 240, 360, 480, and 720 minute halftimes, τ, are employed, and halftimes are independent of pressure. Compartments correlate roughly from brain to bone, that is, fast (few minute halftimes) to slow (few hour halftimes) tissues.

In a series of dives or multiple stages, p_i and p_a represent extremes for each stage, or more precisely, the initial tension and the arterial tension at the beginning of the next stage. Stages are treated sequentially, with finishing tensions at one step representing initial tensions for the next step, and so on. To maximize the rate of uptake or elimination of dissolved gases the *gradient*, simply the difference between p_i and p_a, is maximized by pulling the diver as close to the surface as possible. Exposures are limited by requiring that the tissue tension never exceed M, written,

$$M = M_0 + \Delta M\ d$$

as a function of depth, d, for ΔM the change per unit depth. A set (USN) of M_0 and ΔM are fitted below [10,41,70,71] for nitrogen,

$$M_0 = 152.7\tau^{-1/4}\ fsw$$

$$\Delta M = 3.25\tau^{-1/4}$$

which can be contrasted with the original Haldane constant ratio critical tension, M, recognizable as the $2 - to - 1\ law$ [8,87],

$$M = 1.58P$$

In absolute units, the corresponding critical gradient, G, is given by,

$$G = \frac{M}{0.79} - P$$

with P ambient pressure, and M critical nitrogen pressure. Similarly, the critical ratio, R, takes the form,

$$R = \frac{M}{P}$$

The staging regimen is the usual,

$$p \leq M$$

In lowest order, critical tensions for helium are the same, with helium halftimes, τ_{He}, 2.65 times faster than nitrogen halftimes, τ_{N_2}, that is, by Graham's law [19,81,87],

$$\tau_{He} = \frac{\tau_{N_2}}{2.65}$$

for the same compartments.

At altitude [8,14,27,61,64,76,81], some critical tensions have been correlated with actual testing, in which case, the depth, d, is defined in terms of absolute pressure, P,

$$d = P - P_z$$

with surface pressure, P_z, at altitude, z, given by (fsw),

$$P_z = 33\ exp\ (-0.0381z) = 33\alpha^{-1}$$

$$\alpha = exp\ (0.0381z)$$

and z in multiples of 1,000 feet. However, in those cases where the critical tensions have not been tested nor extended to altitude, an exponentially decreasing extrapolation scheme, called *similarity*, has been employed. Extrapolations of critical tensions, below $P = 33\ fsw$, then fall off more rapidly then in the linear case [23,82,83]. The similarity extrapolation holds the ratio, $R = M/P$, constant at altitude. Denoting an equivalent sea level depth, δ, at altitude, z, one has for an excursion to depth d,

$$\frac{M(d)}{d + 33\alpha^{-1}} = \frac{M(\delta)}{\delta + 33}$$

so that the equality is satisfied when,

$$\delta = \alpha d$$

$$M(\delta) = \alpha M(d).$$

Considering the minimum surface tension pressure of bubbles, G^{min} (near 10 fsw), as a limit point, the similarity extrapolation is usually limited to 10,000 feet in elevation, and neither for decompression, nor heavy repetitive diving.

In the bulk diffusion case, depth-time exposures can be limited by a law of the form [38,81],

$$dt_n^{1/2} = H$$

with t_n the nonstop time limit, and $400 \leq H \leq 500\ fsw\ min^{1/2}$. One can obtain the corresponding tissue constant, λ, controlling the exposure at depth d, for nonstop time t_n, by differentiating the MTM tissue equation with respect to depth, d, and setting the result to zero. With $p_a = 0.79(d+33)$ at sea level, there results,

$$1 - exp\ (-\lambda t_n)(1 + 2\lambda t_n) = 0.$$

Corresponding critical tensions, M, are then easily obtained using d, λ, and t_n. In the above case, the transcendental equation is satisfied when,

$$\lambda t_n = 1.25$$

Time remaining before a stop, time at a stop, or surface interval before flying can all be obtained by inverting the tissue equation. Denoting the appropriate critical tension at some desired stage, M, and the instantaneous tension at that time, p, at stage, p_a, the time remaining, t_r, follows from,

$$t_r = \frac{1}{\lambda} \ln \left[\frac{p - p_a}{M - p_a} \right]$$

for each compartment, λ. Then, the smallest t_r controls the ascent.

The MTM is an icon in world diving circles, forming the basis for released recreational and technical dive tables, commercial protocols, and military diving. It is encoded into many Haldanian decompression meters, particularly before 1995. World Navies have performed extensive wet testing and collected data for MTM correlations and tables, using the staging paradigm of bringing the diver as close to the surface as possible. The critical tensions, M, form a springboard for neo-Haldanian models after 1990.

Split Phase Gradient Model (SPGM)

Multitissue models address dissolved gas transport with saturation gradients driving the elimination. In the presence of free phases, free-dissolved and free-blood elimination gradients can compete with dissolved-blood gradients. One suggestion is that the gradient be split into two weighted parts, the free-blood and dissolved-blood gradients, with the weighting fraction proportional to the amount of separated gas per unit tissue volume. Use of a split phase gradient is consistent with multiphase flow partitioning, and implies that only a portion of tissue gas has separated, with the remainder dissolved. Such a split representation can replace any of the gradient terms in tissue response functions, as suggested and implemented by Wienke, Hills, and others [2,16,29,42,63,69,81].

Accordingly, in the split phase gradient model (SPGM), we write the rate equation, given free phase and tissue partition fractions, γ_p and γ_t, in unit tissue volume, as,

$$\frac{\partial(p - p_a)}{\partial t} = -\gamma_t \lambda (p - p_a) - \gamma_p \frac{\partial(p - P - \delta)}{\partial t}$$

with internal pressure inside the free phase (bubbles), p_b, given by,

$$p_b = P + \delta$$

for δ constrictive surface tension of the separated phase assembly, and P ambient pressure. The above equation cannot be inverted directly for solution, but numerical techniques can be easily applied, as the equation is a linear, first order, differential equation. Specification of free-dissolved gradient, $p - p_b$, and the surface tension, δ, requires knowledge of the dynamics of free phases in tissue and blood, or at least plausible assumptions about bubble kinetics, bubble numbers, and bubble film

structures, taken up next. To schedule decompression, critical tensions, critical free phase volumes, or combinations thereof, can be employed. The partition fractions normalize to one,

$$\gamma_p + \gamma_t = 1$$

and the staging protocol is written generally [82,87],

$$p \leq \alpha M + \beta V$$

for constants,

$$0 \leq \alpha \leq 1$$

$$0 \leq \beta \leq (1 - \alpha)\frac{M}{V_i}$$

with V the estimated phase volume, V_i, the nonexcited phase volume, and M the dissolved gas critical tension.

The SPGM forms a basis for neo-Haldanian decompression meters and commercial software. It can be imbedded into any MTM to yield deep stops. User choice of conservancy factors relate directly to α and β, for given M and estimated V and V_i. Parameters are proprietary mostly, but decompression meters employ the approach. Like the ASTM, the SPGM is found in commercially marketed software offering neo-Haldanian staging alternatives for dive planning.

Linear-Exponential Model (LEM)

Asymmetric uptake and elimination of dissolved gas can also be tracked by using different tissue functions for uptake and elimination. The linear-exponential model (LEM) employs exponential uptake and linear-exponential elimination tissue functions [70,71]. The end result for tissues with the same perfusion rates is a slower outgassing rate versus uptake rate. That is, simply, for inert gas uptake, the rate equation is as before, with τ a characteristic tissue-blood flow time scale, not necessarily arbitrary halftimes as assigned in the MTM and other models,

$$\frac{\partial(p - p_a)}{\partial t} = -\tau^{-1}(p - p_a)$$

with solution, $p = p_i$ at $t = 0$, for p_a arterial partial pressure,

$$(p - p_a) = (p_i - p_a)\ exp\ (-\tau^{-1}t)$$

At some tissue tension, p_c, outgassing is *clamped*, so that the difference between the tissue and arterial tensions is constant. In that case, gas elimination on decompression is assumed to be linear until some later time in the ascent when bubbles are assumed ameliorated, and the elimination is switched back into exponential mode.

$$\frac{\partial p}{\partial t} = -\tau^{-1}(p_c - p_a)$$

Solution, $p = p_c$ at $t = 0$, is now,

$$p = -\tau^{-1}(p_c - p_a)t + p_c$$

The clamping is usually applied early in the decompression. In the LEM, the time constant, λ, is not necessarily linked to any halftime, τ, but carries the same inverse time units. Without loss of generality, we write,

$$\lambda = \frac{1}{\tau}$$

with τ a representative perfusion rate time parameter. One useful form is given by,

$$\lambda = \tau^{-1} = \frac{dq}{dt}\frac{\pi_b}{\pi_t}$$

with dq/dt the blood perfusion rate in unit tissue volume, and π_t and π_b the partition fractions of tissue and blood in that same volume. For well perfused (aqueous) tissue, $\pi_b > \pi_t$, while for poorly perfused (fatty) tissue, $\pi_b < \pi_t$.

The LEM has been employed extensively in air and helium diving by the US Navy, using large data sets to correlate parameters with DCS incidence rates and risk.

Asymmetric Tissue Model (ASTM)

If gas nuclei are entrained in the circulatory system, blood perfusion rates are effectively lowered, an impairment with impact on gas exchange processes. This suggests a possible lengthening of tissue halftimes for elimination over those for uptake. For instance, a 10 min compartment for uptake becomes a 12 min compartment on elimination. Such lengthening procedure and the split elimination gradient render gas uptake elimination asymmetric. Instead of exponential uptake and elimination, exponential uptake and quadratic or linear elimination tissue loading functions can be used. Such modifications can be employed in any perfusion model, and tuned to the data. Such approaches are used in many decompression meters and dive planning software [81,86].

The approach in the asymmetric tissue model (ASTM) is simple. Outgassing halftimes, τ_{out}, are slower than ingassing halftimes, τ_{in}, by inverse fractions, β, that is,

$$\tau_{out} = \beta^{-1}\tau_{in}$$

for given ingassing halftimes, τ_{in}, with,

$$0.0 < \beta \leq 1.0$$

Equivalently, the decay constants are linked,

$$\lambda_{out} = \beta\lambda_{in}$$

Meters and software usually limit β roughly as,

$$0.3 \leq \beta \leq 1.0$$

with large decompression debts incurred in the slow compartments when $\beta < 0.30$, or so. The tissue equation for ingassing is the usual,

$$(p - p_a) = (p_i - p_a)\ exp\ (-\lambda_{in}t)$$

while the outgassing equation uses outgassing constants,

$$(p - p_a) = (p_i - p_a)\ exp\ (-\lambda_{out}t)$$

Ingassing occurs whenever,

$$p < p_a$$

while outgassing occurs in the opposite case,

$$p > p_a$$

Certainly, some compartments are outgassing during a dive while others are ingassing, and vice-versa. Staging maintains the tensions below critical values,

$$p \leq M$$

The effect of slower outgassing on the NDLs is easy to quantify for single exposure dives. If the symmetric NDLs are denoted, t_n, then the shorter (asymmetric elimination) NDLs, denoted t_{nn}, are simply reduced by β at depth, d, that is,

$$t_{nn} = \beta t_n$$

While this simple relationship holds for nonstop exposures, a generalization to multilevel, mixed gas switch, repetitive, reverse profile, and decompression diving is nonexistent. The ASTM is employed in many neo-Haldanian decompression meters today. For a given set of critical tensions, M, in any MTM, the ASTM will always be more conservative because outgassing is slower. In meters, user conservancy knobs are controlled through β.

Dual phase diving algorithms are rather recent innovations, coming online in the past 20 years or so. They are different than dissolved gas algorithms, because they couple dissolved gases to bubbles, and lead to deeper staging as a result. Meters, tables, and software employing these algorithms do exist, and are supplanting traditional models.

Thermodynamic Model (TM)

The thermodynamic model (TM) couples both the tissue diffusion and blood perfusion equations [41]. Cylindrical symmetry is assumed in the model. From a boundary vascular zone of thickness, a, gas diffuses into the extended extravascular region, bounded by b. If we wrap the DM planar geometry into a hollow cylinder of inner radius, a, and outer radius, b, we generate Krogh geometry [41]. The hollow cylindrical model retains all the features of the planar model, and additionally includes curvature for small a and b, with $l = b - a$. Assigning the same boundary conditions at a and b, namely, the tissue tension, p, equals the arterial tension, p_a, writing the diffusion equation in radial cylindrical coordinates,

$$D\frac{\partial^2 p}{\partial r^2} + \frac{D}{r}\frac{\partial p}{\partial r} = \frac{\partial p}{\partial t}$$

and solving yields,

$$p - p_a = (p_i - p_a)\sum_{n=1}^{\infty} X_n\ U_0(\epsilon_n r)\ exp\ (-\epsilon_n^2 Dt)$$

with X_n a constant satisfying initial conditions, U_0 the cylinder functions, and ϵ_n the eigenvalues satisfying,

$$U_0(\epsilon_n a) = \frac{\partial U_0(\epsilon_n b/2)}{\partial r} = 0$$

Averaging over the tissue region, $a \leq r \leq b$, finally gives,

$$p - p_a = (p_i - p_a)\frac{4}{(b/2)^2 - a^2}\sum_{n=1}^{\infty}\frac{1}{\epsilon_n^2}\frac{J_1^2(\epsilon_n b/2)}{J_0^2(\epsilon_n a) - J_1^2(\epsilon_n b/2)}exp\ (-\epsilon_n^2 Dt)$$

with J_1 and J_0 Bessel functions, order 1 and 0. Typical vascular parameters are bounded roughly by,

$$0 < a \leq 4\ \mu m$$
$$10 \leq b \leq 32\ \mu m.$$

Perfusion limiting is applied as a boundary condition through the venous tension, p_v, by enforcing a mass balance across both the vascular and cellular regions at a,

$$\frac{\partial p_v}{\partial t} = -\kappa(p_v - p_a) - \frac{3}{a}S_p D\left[\frac{\partial p}{\partial r}\right]_{r=a}$$

with S_p the ratio of cellular to blood gas solubilities, κ the perfusion constant, and p_a the arterial tension. The coupled set relate tension, gas flow, diffusion and perfusion, and solubility in a complex feedback loop.

The thermodynamic trigger point for decompression sickness is the volume fraction, χ, of separated gas, coupled to mass balance. Denoting the separated gas partial pressure, P_{N_2}, under worse case conditions of zero gas elimination upon decompression, the separated gas fraction is estimated,

$$\chi P_{N_2} = S_c(p - P_{N_2})$$

with S_c the cellular gas solubility. The separated nitrogen partial pressure, P_{N_2} is taken up by the inherent unsaturation, and given by (fsw),

$$P_{N_2} = P + 3.21$$

in the original Hills [41,42] formulation, but other estimates have been employed. Mechanical fluid injection pain, depending on the injection pressure, δ, can be related to the separated gas fraction, χ, through the tissue modulus, K,

$$K\chi = \delta$$

so that a decompression criteria requires the staging paradigm,

$$K\chi \leq \delta$$

with δ in the range, for $K = 3.7 \times \ 10^4 \ dyne \ cm^{-2}$,

$$0.34 \leq \delta \leq 1.13 \ fsw.$$

Identification of separated phase volume as a critical indicator is a significant development in decompression theory [39]. The TM was correlated with profiles of Australian pearl divers [49] in the Torres Straits, and was sporadically tested in the open ocean. Deep stops are central in the TM to control phase growth, but early dropout in the shallow zone often increases risk. The TM serves as a springboard for bubble models to follow.

Varying Permeability Model (VPM)

Following development of the TM, Yount and co-workers [89-91] turned to decompressed gel studies in the laboratory as a model for bubble growth and control in diving environments. Using a critical volume of bubbles excited into growth following compression-decompression, and gel parameters for excitation radii of bubbles, the varying permeability model (VPM) was constructed. The critical radius, r_i, at fixed pressure, P_i, represents the cutoff for growth upon decompression to lesser pressure. Nuclei larger than r_i will all grow upon decompression. Additionally, following an initial compression, a smaller class of micronuclei of critical radius, r, can be excited into growth with decompression. If r_i is the critical radius at P_i, then, the smaller family, r, excited by decompression from P, obeys,

$$\frac{2\gamma}{r} - P = \frac{2\gamma}{r_i} - P_i$$

with roughly,

$$50.0 \leq \gamma \leq 250.0 \ fsw \ \mu m$$

for P measured in fsw, and r in μm. Excitation radii, r, thus follow,

$$\frac{1}{r} - \frac{1}{r_i} = \frac{P - P_i}{2\gamma}$$

with $r_i = 0.8 \ \mu m$ at $P_i = 33 \ fsw$. The minimum excitation gradient, G^{min}, initially probing r, and taking into account generation of nuclei over time scales τ_r, is (fsw),

$$G^{min} = \frac{2\gamma \ (\gamma_c - \gamma)}{\gamma_c \ r(t)} = \frac{11.01}{r(t)}$$

with,

$$r(t) = r + (r_i - r) \ [1 - exp \ (-\lambda_r t)]$$

γ, γ_c film, surfactant surface tensions, that is, $\gamma = 17.9\ dyne/cm$, $\gamma_c = 257\ dyne/cm$, and λ_r the inverse of the generation time for stabilized gas micronuclei (many days). Prolonged exposure leads to saturation, and the largest permissible gradient, G^{sat}, takes the form (fsw), in all compartments,

$$G^{sat} = \frac{58.6}{r} - 49.9 = 0.372\ P + 11.01.$$

On the other hand, G^{min} is the excitation threshold, the amount by which the surrounding tension must exceeed internal bubble pressure to just support growth. Although the actual size distribution of gas nuclei in humans is unknown, experiments *in vitro* suggest that a decaying exponential is reasonable,

$$n = N\ exp\ (-\beta r)$$

with β a constant, and N a convenient normalization factor across the distribution. For small values of the argument, βr,

$$exp\ (-\beta r) = 1 - \beta r$$

as a nice simplification. For a stabilized distribution, n_0, accommodated by the body at fixed pressure, P_0, the excess number of nuclei, Λ, excited by compression-decompression from new pressure, P, is,

$$\Lambda = n_0 - n = N\beta r_i \left[1 - \frac{r}{r_i}\right].$$

For large compressions-decompressions, Λ is large, while for small compressions-decompressions, Λ is small. When Λ is folded over the gradient, G, in time, the product serves as a critical volume indicator and can be used as a limit point in the following way.

The rate at which gas grows in tissue depends upon both the excess bubble number, Λ, and the gradient, G. The critical volume hypothesis requires that the integral of the product of the two must always remain less than some limit point, $\alpha\ V$, with α a proportionality constant,

$$\int_0^\infty \Lambda G dt = \alpha V$$

for V the limiting gas volume. Assuming that gradients are constant during decompression, t_d, while decaying exponentially to zero afterwards, and taking the limiting condition of the equal sign, yields simply for a bounce dive, with λ the tissue constant,

$$\Lambda G\ (t_d + \lambda^{-1}) = \alpha V.$$

In terms of earlier parameters, one more constant, δ, closes the set, defined by,

$$\delta = \frac{\gamma_c \alpha V}{\gamma \beta r_i N} = 7180\ fsw\ min$$

so that,

$$\left[1 - \frac{r}{r_i}\right]\ G\ (t_d + \lambda^{-1}) = \delta \frac{\gamma}{\gamma_c} = 500.8\ fsw\ min.$$

The five parameters, γ, γ_c, δ, λ_r, r_i, are five of the six fundamental constants in the varying permeability model. The remaining parameter, λ_m, interpolating bounce and saturation exposures, represents the inverse time contant modulating multidiving. The depth at which a compartment controls an exposure, and the excitation radius as a function of halftime, τ, in the range, $12 \leq d \leq 220\ fsw$, satisfy,

$$\frac{r}{r_i} = 0.90 - 0.43\ exp\ (-\zeta\tau)$$

with $\zeta = 0.0559\ min^{-1}$. The generation constant, λ_r, is on the order of inverse days, that is, $\lambda_r = .0495\ days^{-1}$. Characteristic halftimes, τ_r and τ_h, take the values $\tau_r = 14\ days$ and $\tau_h = 12.4\ min$. For large τ, r is close to r_i, while for small τ, r is on the order of 0.5 r_i. At sea level, $r_i = 0.8\ \mu m$.

Staging on the allowed tissue supersaturation is linked to the bubble surface pressure,

$$p - P \leq 2\ \frac{\gamma}{\gamma_c r}(\gamma_c - \gamma)$$

with, in the permeable region,

$$r = \left[\frac{(P - P_i)}{2(\gamma_c - \gamma)} + \frac{1}{r_i}\right]^{-1}$$

and, in the impermeable region,

$$r^3 - 2(\gamma_c - \gamma)r^2 - \frac{P_i}{\zeta}r_c^3 = 0$$

for,

$$\zeta = P - 2P_c + 2P_i + \frac{2(\gamma_c - \gamma)}{r_c}$$

according to gel measurements detailed earlier, with P_c near 6 atm. VPM parameters were also fitted to air and helium diving data in shallow zones. The VPM is available in some dive planning software for technical diving.

Reduced Gradient Bubble Model (RGBM)

The RGBM employs a phase volume constraint [81,84,88] across the total dive profile. The gel parameterization is replaced by flexible seed skins with appropriate EOS, permeable to gas diffusion at all pressures and temperatures. Gas diffuses across the bubble interface, and the bubble is subject to Boyle expansion-contraction. The phase volume constraint equation is rewritten in terms of a phase function, $\dot{\phi}$, varying in time,

$$\int_0^\tau \frac{\partial \phi}{\partial t} dt\ \leq\ \Phi$$

with, as before,

$$\dot{\phi} = \frac{\partial \phi}{\partial t}$$

for Φ the separated phase, and τ some (long) cutoff time. More particularly, for Π the total gas tension, taking $\tau \to \infty$, holding temperature constant,

$$\dot{\phi} = \left[\frac{\partial V}{\partial t}\right]_{diffusion} + \left[\frac{\partial V}{\partial t}\right]_{Boyle} + \left[\frac{\partial V}{\partial t}\right]_{excitation}$$

for,

$$\left[\frac{\partial V}{\partial t}\right]_{diffusion} = 4\pi\beta\ exp\ (\beta\epsilon)DS \int_\epsilon^\infty nr \left[\Pi - P - \frac{2\gamma}{r}\right] dr$$

$$\left[\frac{\partial V}{\partial t}\right]_{Boyle} = 4\pi\beta\ exp\ (\beta\epsilon) \int_\epsilon^\infty nr^2 \left[\frac{\partial r}{\partial P}\frac{\partial P}{\partial t}\right] dr$$

$$\left[\frac{\partial V}{\partial t}\right]_{excitation} = 4\pi \frac{\partial}{\partial t}\left[\theta(t - t_{ex}) \int_\epsilon^\infty nr^2 dr\right]$$

with all quantities as denoted previously, the seed density normalized to the excited seed volume, V,

$$4\pi \int_\epsilon^\infty nr^2 dr = 4\pi \int_\epsilon^\infty exp\ (-\beta r) r^2 dr = V$$

the heaviside function, θ, defined for seed excitation at time, t_{ex},

$$\theta(t - t_{ex}) = 0, \quad t \leq t_{ex}$$

$$\theta(t - t_{ex}) = 1, \quad t > t_{ex}$$

with the time derivative of the heaviside function a delta function,

$$\frac{\partial \theta(t - t_{ex})}{\partial t} = \delta(t - t_{ex})$$

To simplify EOS lookups, Boyle factors, ξ, are used, so that,

$$\xi PV = nRT$$

as detailed earlier. Thus the phase function, $\dot{\phi}$, depends on the number of bubbles, n, stimulated into growth by compression-decompression, the supersaturation gradient, G, seed expansion-contraction by radial diffusion, $\partial r/\partial t$, Boyle expansion-contraction with pressure changes, P, and inside temperature, T, in general. The excitation radius [16,22,29], ϵ, depends on the material properties [24,92], and is taken for nitrogen (μm),

$$\epsilon_{N_2} = 0.007655 + 0.001654 \left[\frac{T}{P}\right]^{1/3} + 0.041602 \left[\frac{T}{P}\right]^{2/3}$$

and for helium,

$$\epsilon_{He} = 0.003114 + 0.015731 \left[\frac{T}{P}\right]^{1/3} + 0.025893 \left[\frac{T}{P}\right]^{2/3}$$

for T measured in absolute ^oK, and P given in fsw, with ranges for virial coefficients, aqueous to lipid materials, varying by factors of 0.75 to 4.86 times the values listed above. Both expressions obtain from fits to RGBM mixed gas data across lipid and aqueous bubble films, and are different from other phase models. Values of excitation radii, ϵ, above range from 0.01 to 0.05 μm for sea level down to 500 fsw. This is compared to excitation radii in other models (VPM and TBDM) which vary in the 1 μm range. In the very large pressure limit, excitation radii (like beebees) are in the 1/1,000 μm range. Table 2 lists excitation radii (air) according to the RGBM.

Table 2. RGBM Excitation Radii

pressure P (fsw)	excitation radius ϵ (μm)	pressure P (fsw)	excitation radius ϵ (μm)
13	0.174	153	0.033
33	0.097	183	0.029
53	0.073	283	0.024
73	0.059	383	0.016
93	0.051	483	0.011
113	0.046	583	0.009

To track Boyle bubble expansion-contraction easily, a set of multipliers, ξ, is tabulated in Table 3 below. For changes in pressure, P, we have,

$$\xi_i P_i V_i = \xi_f P_f V_f$$

as before, with i and f denoting initial and final states. Multipliers represent a 50/50 lipid-aqueous skin, following Sears [62], Eisenberg [28], Cottrell [24].

Table 3. RGBM Boyle Multipliers

depth (fsw)	EOS multiplier ξ
30	0.610
90	0.732
150	0.859
210	0.939
270	1.032
330	1.119
390	1.169
450	1.183
510	1.203

To track gas transfer across bubble boundaries, we need mass transport coefficients, DS, for inert gases. Table 4 lists DS for the same lipid-aqueous surfaces, using Eisenberg [28], Frenkel [33], and Bennett and Elliot [10],

Table 4. RGBM Mass Transfer Coefficients

gas	DS ($\mu m^2/sec\ fsw$)
H_2	72.5×10^{-6}
He	18.4×10^{-6}
Ne	10.1×10^{-6}
N_2	56.9×10^{-6}
Ar	40.7×10^{-6}
O_2	41.3×10^{-6}

Notice that helium has a low mass transport coefficient, some 3 times smaller than nitrogen. Two parameters, closing the set, are nominally (STP),

$$\Phi = 840\ \mu m^3$$

$$\beta = 0.6221\ \mu m^{-1}$$

fitted to collected (LANL Data Bank) deep, mixed gas, decompression data [80], and with varying bubble surface tension [26,33],

$$2\gamma = 44.7 \left[\frac{P}{T}\right]^{1/4} + 24.3 \left[\frac{P}{T}\right]^{1/2}\ dyne/cm$$

The inherent unsaturation (oxygen window), υ, takes the form (fsw),

$$\upsilon = f_{O_2} P - 4.87$$

with P ambient pressure, and f_{O_2} oxygen fraction. Under compression-decompression, some of this window takes up inert gases, denoted, ζ,

$$\zeta = f_{O_2} P - \upsilon$$

Staging in the RGBM requires the supersaturation gradient to remain under the seed averaged bubble surface pressure,

$$p - P \leq \beta\ exp\ (\beta\epsilon) \int_{\epsilon}^{\infty} exp\ (-\beta r) \frac{2\gamma}{r} dr$$

whereby the seed distribution controls the ascent.

Two linked bubble algorithms exist. One is a folded algorithm using phase factors from the full iterative model to limit repetitive, reverse profile, multiday activities, and flying after diving using $M - values$. Detailed next, it is called the modified gradient phase model (MGPM). It uses results from the RGBM to deduce phase factors for folding. Both are correlated with data in the LANL Data Bank (2843 profiles and 18 cases of DCS). The folded version is found in many decometers on the market today. It is mainly employed in the recreational air and nitrox arenas. The bubble version above is the basis of released mixed gas decompression tables and simplified no-group, no-calc recreational air and nitrox tables up to 10,000 ft elevation. Meter implementations of the full RGBM are available and under continuing development. The full up RGBM described above is employed in the technical, research, and scientific diving communities. It is a mainstay for LANL operations, and is used now in the commercial, oil patch, sector. Decompression meters and dive planning software are readily available with the algorithm.

Modified Gradient Phase Model (MGPM)

Classical approaches use a dissolved gas (tissue) transfer equation, and a set of critical parameters to dictate diver staging through the gas transfer equation. In the Workman [10,41,81] approach, the critical parameters are called $M - values$, while in the Buhlmann [10,19,81] formulation they are called a and b. They are equivalent sets, slightly different in representation but not content. Consider air, nitrox, heliox, and trimix in the ZHL formalism [19,44,85].

Staging is controlled in the ZHL algorithm through sets of tissue parameters, a and b, listed below in Table 5 for 14 tissues, τ, through the minimum permissible (tolerable) ambient pressure, P_{min}, by,

$$P_{min} = (p - a)b$$

across all tissue compartments, τ, with the largest P_{min} limiting the allowable ambient pressure, P_{min}.

Table 5. Nitrogen ZHL Critical Parameters (a, b)

halftime τ (min)	critical intercept a (bar)	critical slope b
5.0	1.198	0.542
10.0	0.939	0.687
20.0	0.731	0.793
40.0	0.496	0.868
65.0	0.425	0.882
90.0	0.395	0.900
120.0	0.372	0.912
150.0	0.350	0.922
180.0	0.334	0.929
220.0	0.318	0.939
280.0	0.295	0.944
350.0	0.272	0.953
450.0	0.255	0.958
635.0	0.236	0.966

In terms of critical tensions, M, according to the USN, the relationship linking the two sets is simply,

$$M = \frac{P}{b} + a = \Delta M \ P + M_0$$

so that,

$$\Delta M = \frac{1}{b}$$

$$M_0 = a$$

in units of bar, though the usual representation for M is fsw. The above set, a and b, hold generally for nitrox, and, to low order, for heliox (and trimix too). Tuned modifications for heliox and trimix are tabulated below. According to the MGPM, bubble-like model behavior within critical parameters, a, b, is established through multidiving reduction factors, f, such that for any set of nonstop gradients, G,

$$G = M - P$$

a reduced set, G_f, obtains from the nonstop set, G, for multidiving through the reduction factors, $f \leq 1$,

$$G_f = fG$$

so that,

$$M_f = \frac{P}{b_f} + a_f = G_f + P = fG + P$$

but, since,

$$fG = f(M - P) = f\left[\left(\frac{P}{b}\right) + a - P\right]$$

we have,

$$a_f = fa$$

$$b_f = \frac{b}{f(1-b)+b}$$

The new (reduced) staging regimen is then simply,

$$P_{min} = (p - a_f)b_f$$

using *reduced* critical parameters, a_f and b_f. Certainly, as $f \rightarrow 1$, then $a_f \rightarrow a$, and $b_f \rightarrow b$, as requisite. Now all that remains is specification of f, particularly in terms of repetitive, reverse profile, and multiday diving, as limited by the bubble dynamical RGBM. The full factor, f, depends on tissue halftime, τ, generally through the relationship (for nitrox),

$$f = (1 - f_0)\ \frac{\tau}{180} + f_0 \quad (f = 1, \ \ \tau \geq 180\ min)$$

as the tissue scaling up through the 180 min nitrogen compartment, with multdiving weighting,

$$f_0 = 0.45\ f_{rp} + 0.30\ f_{dp} + 0.25\ f_{dy}$$

where f_{rp}, f_{dp}, and f_{dy} are reduction factors for repetitive, reverse profile (deeper than previous), and multiday (time spans of 30 hrs or more) diving. These forms for multidiving f are dependent on time between dives, t_{sur}, maximum ambient pressure difference on reverse profile dives, $(\Delta P)_{max}$, maximum ambient pressure, P_{max}, and multiday diving frequency, n, over 24 hr time spans. Specifically, they are written [84,87],

$$f_{rp} = 1 - 0.45\ exp\ \left[-\frac{(t_{sur} - \eta_{rp})^2}{4\eta_{rp}^2}\right]$$

$$10\ min \leq \eta_{rp} \leq 90\ min$$

$$f_{dp} = 1 - 0.45\ \left[1 - exp\ \left(-\frac{(\Delta P)_{max}}{P_{max}}\right)\right]\ exp\ \left[-\frac{(t_{sur} - \eta_{dp})^2}{4\eta_{dp}^2}\right]$$

$$30\ min \leq \eta_{dp} \leq 120\ min$$

$$f_{dy} = .70 + .30\ exp\ \left(-\frac{n}{\eta_{dy}}\right)$$

$$12\ hrs \leq \eta_{dy} \leq 18\ hrs$$

with t_{sur} measured in min, and n the number of consecutive days of diving within 30 hr time spans. These factors are applied after 1 min of surface interval (otherwise, previous dive continuation). The difference, $(\Delta P)_{max}$, can be the time averaged difference between depths on the present and previous dives (computed on the fly). Fits using collected data (LANL Data Bank) cross reference RGBM and MGPM parameters for recreational and light decompression diving.

The standard set, a, b, and τ is modified for helium mixtures, with basic change in the set of halftimes, τ, used for the set, a and b. To lowest order, a and b for helium are the same as those for nitrogen, though we will list the modifications in Table 6 below. Halftimes for helium are approximately 2.65 times faster than those for nitrogen, by Graham's law (molecular diffusion rates scale inversely with square root of atomic masses). That is,

$$\tau_{He} = \frac{\tau_{N_2}}{2.65}$$

because helium is approximately 7 times lighter than nitrogen, and diffusion rates scale with square root of the ratio of atomic masses. The tissue equation is the same as the nitrox tissue equation, but with helium constants, λ, defined by the helium tissue halftimes. Multidiving fractions are the same, but the tissue scaling is different across the helium set,

$$f = (1 - f_0)\ \frac{\tau}{67.8} + f_0 \quad (f = 1,\ \ \tau \geq 67.8\ min)$$

and all else is the same.

Table 6. Helium ZHL Critical Parameters (a, b)

halftime τ (min)	critical intercept a (bar)	critical slope b
1.8	1.653	0.461
3.8	1.295	0.604
7.6	1.008	0.729
15.0	0.759	0.816
24.5	0.672	0.837
33.9	0.636	0.864
45.2	0.598	0.876
56.6	0.562	0.885
67.8	0.541	0.892
83.0	0.526	0.901
105.5	0.519	0.906
132.0	0.516	0.914
169.7	0.510	0.919
239.6	0.495	0.927

For trimix, both helium and nitrogen are tracked with tissue equations, and appropriate average of helium and nitrogen critical parameters used for staging. Denoting nitrogen and helium fractions, f_{N_2}, and f_{He}, ambient nitrogen and helium pressures, p_{aN_2} and p_{aHe}, tissue halftimes are mapped exactly as listed in Tables 5 and 6, and used appropriately for nitrogen and helium tissue equations. Additionally,

$$f_{O_2} + f_{N_2} + f_{He} = 1$$

Total tension is the sum of nitrogen and helium tensions. Critical parameters for trimix, α_f and β_f, are just weighted averages of critical parameters, a_{N_2}, b_{N_2}, a_{He} b_{He}, from Tables 3 and 4, that is, generalizing to the reduced set, a_f and b_f,

$$\alpha_f = \frac{f_{N_2} a_{fN_2} + f_{He} a_{fHe}}{f_{N_2} + f_{He}}$$

$$\beta_f = \frac{f_{N_2} b_{fN_2} + f_{He} b_{fHe}}{f_{N_2} + f_{He}}$$

The staging regimen for trimix is,

$$P_{min} = (\Pi - \alpha_f)\beta_f$$

as before. The corresponding critical tension, M_f, generalizes to,

$$M_f = \frac{P}{\beta_f} + \alpha_f$$

Obviously, the above set of equations include any mixture of nitrogen, helium, and oxygen (air, nitrox, heliox, trimix), The MGPM is employed is used extensively in neo-Haldanian decompression meters.

Tissue Bubble Diffusion Model (TBDM)

Bubbles shrink or grow according to a simple radial diffusion equation linking total gas tension, Π, ambient pressure, P, and surface tension, γ, to bubble radius, r,

$$\frac{\partial r}{\partial t} = \frac{DS}{r}\left[\Pi - P - \frac{2\gamma}{r}\right]$$

with D the gas diffusion coefficient, and S the gas solubility. Bubbles grow when the surrounding gas tension exceeds the sum of ambient plus surface tension pressure, and vice-versa. Higher gas solubilities and diffusivities enhance the rate. Related bubble area, A, and volume, V, changes satisfy,

$$\frac{\partial A}{\partial t} = 8\pi r \frac{\partial r}{\partial t}$$

$$\frac{\partial V}{\partial t} = 4\pi r^2 \frac{\partial r}{\partial t}$$

Using Fick's law, a corresponding molar current, J, of gas into, or out of, the bubble is easily computed assuming an ideal gas,

$$J = -\frac{DS}{RTh}\left[\Pi - P - \frac{2\gamma}{r}\right]$$

for R the ideal gas constant, T the temperature, and h an effective diffusion barrier thickness. And the molal flow rate is just the molal current times the interface area, that is,

$$\frac{\partial n}{\partial t} = JA$$

for n the number of moles of gas. The change in pressure and volume of the bubble, due to gas diffusion, follows simply from the ideal gas law,

$$\frac{\partial (PV + 2\gamma r^{-1} V)}{\partial t} = R\frac{\partial (nT)}{\partial t}$$

for V the bubble volume.

Obviously, the above constitute a coupled set of differential equations, solvable for a wide range of boundary and thermodynamic conditions connecting the state variables, namely, P, V, Π, r, n, and T. In the Gernhardt [35] treatment, tissue deformation, ξ, is given by,

$$\xi = \frac{4}{3}\pi r^3 Y$$

with Y the tissue bulk modulus, and r the bubble radius. Staging can be applied by limiting tissue deformation, such that symbolically,

$$\xi \leq \frac{4}{3}\pi r^3 Y_{min}$$

Bubble dose, based on the hypothetical volume of an expanding test bubble, can also be linked to staging for any exposure. Maximum likelihood regression is used to correlate bubble dose parameters with DCS risk. Staging can be then correlated with dose and risk. This approach is likely employed in the commercial diving sector.

Linear-Exponential Phase Model (LEPM)

Thalmann and others [70,71,75] have extended USN dissolved gas models to emulate bubble behavior, using both (either) modified $M-values$ or separated bubble volumes, as critical staging parameters. The model enjoys correlation with extensive US Navy data sets accumulated over the years, and is based on statistics gathered for dissolved gas staging but not necessarily deep stops, likely a data-model mismatch.

In the LEPM, the assumption that gas content remains in solution at all times during decompression is relaxed to acommodate gas bubble formation and growth. Under this relaxation, mass balance equates the rate of change of tissue compartment dissolved gas tension to the rate of gas uptake from the blood minus the gas flux into the bubbles. In essence, this is congruent with the split phase gradient model (SPGM) discussed previously. The particular form of the transfer rate equation is,

$$\frac{\partial p}{\partial t} = \frac{p_a - p}{\tau} - \frac{1}{\alpha_t V}\sum_{n=1}^{N}\frac{\partial (P_n V_n)}{\partial t}$$

with N the number of bubbles, P_n the inert gas pressure in the n^{th} bubble, V_n the volume of the n^{th} bubble, V the compartment total volume, α_t the tissue partition fraction, and τ the time constant. In the absence of bubbles, the last term vanishes, and the LEM equations are recovered.

Unlike the kinetics of exponential uptake and elimination, regardless of compartment saturation, the linear exchange kinetics of the LEM and LEPM via arterial-tissue tension clamping occur once bubbles are assumed to form. While this exact time is not known, the US Navy approach assumes bubble formation when a set of reduced critical tensions, denoted M_r to distinguish them from classical $M-values$ of multitissue models, are exceeded. The bubble growth term, $\partial V/\partial t$, has no seed dynamics imbedded in its definition (unlike RGBM and VPM), but proceeds according to an expression suggested by Van Liew [73,74]. For r the bubble radius, and all other quantities as defined before, the growth rate is,

$$\frac{\partial V}{\partial t} = -4\pi r^2 \alpha_t D_t \left[1 - \frac{p}{p_b}\right]\left[\delta + \frac{1}{r}\right]$$

with p tissue tension, p_b reduced bubble internal pressure (active gas partial pressures subtracted from ambient pressure),

$$p_b = P - p_{H_2O} - p_{CO_2} - p_{O_2} + \frac{2\gamma}{r}$$

for D_t compartmental bulk diffusion coefficient, and δ a penetration length,

$$\delta^2 = \frac{dQ}{dt}\,\frac{\alpha_b}{\alpha_t D_t V_t}$$

within tissue volume, V_t. Boyle effects occur instantaneously with changes in ambient pressure, P, as in in other bubble models. Staging is effected through the reduced critical tensions,

$$p \leq M_r$$

as a portion of the dissolved gas is assumed to phase transition. As in the dissolved gas LEM, extensive correlations with USN data are linked to the LEPM, and the model is under continuing analyses.

Summary

Bubble measurements, wet and dry testing, data collection and analyses, and dual phase models have spawned some new protocols, worth enumerating at this point, as far as impact on operational diving [10,12,30,31,39,44,47-49,52,57,66,69,79,83,85]:

1. reduced nonstop time limits;
2. safety stops (or shallow swimming ascents) in the 10-20 fsw zone;
3. ascent rates not exceeding 30 fsw/min;
4. restricted repetitive exposures, particularly beyond 100 fsw,
5. restricted reverse profile and deep spike diving;
6. restricted multiday activity;
7. smoother coalescence of differring algorithm limit points;
8. consistent diving protocols for altitude;
9. deep stops for decompression, extended range, and mixed gas diving with overall shorter decompression times, particularly for the shallow zone;
10. use of helium rich mixtures for technical diving, with shallow isobaric switches to nitrox (above 70 fsw roughly);
11. use of pure oxygen in the shallow zone to eliminate both dissolved and bubble inert gases.

These are fairly recent developments on the diving scene, with seemingly no spikes in DCS incidence rates reported within categories of divers employing them. Yet certainly, few of these procedures have been tested, particularly in the deep, decompression, and mixed gas diving zones. In time, many procedures will be tested or analyzed with growing profile data, and protocols validated, modified, or discarded. Of course, wet and dry testing are expensive, limited in range, and not always viable operationally. In that respect, profile data banks with diver outcomes are enormously important to cover a full spectrum of diving not amenable nor feasible for wet and dry testing. The profile data banks at DAN [64] and LANL [80] are two modern ones, with DAN focused on recreational diving and LANL concerned with technical deep, mixed gas, and decompression diving. To say these data banks can help fill holes in the testing arena might be an understatement.

REFERENCES

1. *Arndt R.E.A. and Ippen A.T., 1968, Rough Surface Effects On Cavitation Inception, ASME J. Basic Eng. 90, 249-261.*

2. *Ball R., Himm J.F., Homer L.D., and Thalmann E.D., 1994, Model Of Bubble Evolution During Decompression Based On A Monte Carlo Simulation Of Inert Gas Diffusion, Naval Medical Research Institute Report, NMRI 94-36, Bethesda.*

3. *Batchelor G.K., 1953, Theory Of Homogeneous Turbulence, New York: Cambridge University Press.*

4. *Bateman J.B. and Lang J., 1945, Formation And Growth Of Bubbles In Aqueous Solutions, Canad. J. Res. E23, 22-31.*

5. *Becker R. and Doring W., 1965, The Kinetic Treatment Of Nuclei Formation In Supersaturated Vapors, Ann. Phys. 24, 719-752.*

6. *Behnke A.R., 1971, Decompression Sickness: Advances And Interpretations, Aerospace Med. 42, 255-267.*

7. *Behnke A.R., 1967, The Isobaric (Oxygen Window) Principle Of Decompression, Trans. Third Annual Conf. Marine Tech, Soc. 1, 213-228.*

8. *Behnke A.R., 1945, Decompression Sickness Incident To Deep Sea Diving And High Altitude, Medicine 24, 381-402.*

9. *Benjamin T.B. and Ellis A.T., 1966, The Collapse Of Cavitation Bubbles Under Pressure Produced By Solid Boundaries, Trans. Royal Soc. A260, 221-240.*

10. *Bennett P.B. and Elliot D.H., 1993, The Physiology And Medicine Of Diving And Compressed Air Work (4th Edition), London: Bailliere Tindall And Cassell.*

11. *Bennett P.B. and Hayward A.J., 1968, Relative Decompression Sickness In Rats Of Neon And Other Inert Gases, Aerospace Med. 39, 301-302.*

12. *Berghage T.E. and Durman D., 1980, US Navy Air Recompression Schedule Risk Analysis, Nav. Med. Res. Bull. 1, 1-22.*

13. *Blank M., 1979, Monolayer Permeability, Prog. Surface Mem. Science, 13, 87-139.*

14. *Boni M., Schibli R., Nussberger P. and Buhlmann A. A., 1976, Diving At Diminished Atmospheric Pressure: Air Decompression Tables For Different Altitudes, Undersea Biomed. Res. 3, 189-204.*

15. *Boycott A.E., Damant G.C.C., and Haldane J.S., 1908, The Prevention Of Compressed Air Illness, J. Hyg. 8, 342-443.*

16. *Brennen C.E., 1995, Cavitation And Bubble Dynamics, Oxford: Oxford University Press.*

17. *Brubakk A.O., Arntzen A.J., Wienke B.R. and Koteng S., 2003, Decompression Profile And Bubble Formation After Dives With Surface Decompression: Experimental Support For A Dual Phase Model Of Decompression, Undersea Hyper. Med. 30, 181-193.*

18. *Buckles R.G., 1968, The Physics Of Bubble Formation And Growth, Aerospace Med. 39, 1062-1069.*

19. *Buhlmann A.A., 1984, Decompression/Decompression Sickness, Berlin: Springer Verlag.*

20. *Campbell J., 1968, The Tribonucleation Of Bubbles, Brit J. Appl. Phys. 1, 1083-1088.*

21. *Carter L.L. and Cashwell E.D., 1975, Particle Transport Simulations With The Monte Crarlo Method, Oak Ridge: United States Energy And Research Development Administration.*

22. *Clift R., Grace J.R., and Weber M.E., 1978, Bubbles, Drops, And Particles, New York: Academic Press.*

23. *Conkin J. and Van Liew H.D., 1991, Failure Of The Straight Line Boundary Between Safe And Unsafe Decompressions When Extraoplated To The Hypobaric Regime, Undersea Biomed. Res. 18, 16.*

24. *Cottrell A.H., 1964, Mechanical Properties Of Matter, New York: John Wiley And Sons Incorporated.*

25. *Courant R. and Friedrichs K.O., 1948, Supersonic Flow And Shock Waves, New York: John Wiley And Sons Incorporated.*

26. *Crum L.A., 1979, Tensile Strength Of Water, Nature 278, 149-149.*

27. *Egi S.M. and Brubakk A.O., 1995, Diving At Altitude: Review Of Decompression Strategies, Undersea Hyper. Med. 22, 281-300.*

28. *Eisenberg D. and Kautzmann W., 1969, The Structure And Properties Of Water, Oxford: Oxford University Press.*

29. *Epstein P.S. and Plesset M.S., 1950, On The Stability Of Gas Bubbles In Liquid-Gas Solutions, J. Chem. Phys. 18, 1505-1509.*

30. *Evans A. and Walder D.N., 1969, Significance Of Gas Macronuclei In The Aetiology Of Decompression Sickness, Nature 222, 251-252.*

31. *Farm F.P., Hayashi E.M., and Beckman E.L., 1986, Diving And Decompression Sickness Treatment Practices Among Hawaii's Diving Fisherman, University of Hawaii Sea Grant Report, UNIHI-SEAGRANT-TP-86-01, Honolulu.*

32. *Fisher J.C., 1948, The Fracture Of Liquids, J. Appl. Phys. 19, 1062-1067.*

33. *Frenkel J., 1946, Kinetic Theory Of Liquids, New York: Oxford University Press.*

34. *Gernhardt M.L., Lambertsen C.J., Miller R.G., and Hopkins E., 1990, Evaluation Of A Theoretical Model Of Tissue Gas Phase Growth And Resolution During Decompression From Air Diving, Undersea Biomed. Res. 17, 95.*

35. *Gernhardt M.L., 1985, Tissue Gas Bubble Dynamics During Hypobaric Exposures, Society Of Automotive Engineers Report, SAE-851337, Warrendale.*

36. *Harvey E.N., 1945, Decompression Sickness And Bubble Formation In Blood And Tissue, Bull. N.Y. Acad. Med. 21, 505-536.*

37. *Hawkins J.A., Shilling C.W., and Hansen R.A., 1935, A Suggested Change In Calculating Decompression Tables For Diving, USN Med. Bull. 33, 327-338.*

38. *Hempleman H.V., 1952, A New Theoretical Basis For The Calculation Of Decompression Tables, Medical research Council Report, UPS 131, London.*

39. *Hennessy T.R. and Hempleman H.V., 1977, An Examination Of The Critical Released Gas Concept In Decompression Sickness, Proc. Royal Soc. London B197, 299-313.*

40. *Hennessy T.R., 1974, The Interaction Of Diffusion And Perfusion In Homogeneous Tissue, Bull. Math. Biol. 36, 505-527.*

41. *Hills B.A., 1977, Decompression Sickness, New York: John Wiley And Sons Incorporated.*

42. *Hills B.A., 1968, Relevant Phase Conditions For Predicting The Occurrence Of Decompression Sickness, J. Appl. Physiol. 25, 310-315.*

43. *Ikels K. G., 1970, Production Of Gas Bubbles In Fluids By Tribonucleation, J. Appl. Physiol. 28, 524-527.*

44. *Keller H. and Buhlmann A.A., 1965, Deep Diving And Short Decompression By Breathing Mixed Gases, J. Appl. Physiol. 20, 1267.*

45. *Knapp R.T., Daily J.W., and Hammitt F.G., 1970, Cavitation And Bubbles, New York: McGraw-Hill Book Company.*

46. *Kunkle T.D. and Beckman E.L., 1983, Bubble Dissolution Physics And The Treatment Of Decompression Sickness, Med. Phys. 10, 184-190.*

47. *Lambertsen J.L. and Bornmann R.C., 1979, Isobaric Inert Gas Counterdiffusion, Undersea And Hyperbaric Medical Society Publication 54WS(IC)1-11-82, Bethesda.*

48. *Lehner C.E., Lin T.F., Taya F., Wienke B.R., Nordheim E.V., Cuddon P.A., and Lanphier E.H., 1994, Acclimatization Reduces The Incidence Of Decompression Sickness: A Sheep Model, Undersea Hyper. Med. 21, 22.*

49. *Le Messurier D.H. and Hills B.A., 1965, Decompression Sickness: A Study Of Diving Techniques In The Torres Strait, Hvaldradets Skrifter 48, 54-84.*

50. *Mulhearn P.J., 1981, Distribution Of Microbubbles In Coastal Waters, J. Geophys. Res. 86, 6429-6434.*

51. *Neimark A.V. and Vishnaykov A., 2005, Monte Carlo Simulation Study Of Droplet Formation, J. Chem. Phys. 122, 1-10.*

52. *Neuman T.S., Hall D.A. and Linaweaver P.G., 1976, Gas Phase Separation During Decompression In Man, Undersea Biomed. Res. 7, 107-112.*

53. *Nishi R.Y., 1991, Development Of Surface Decompression Tables For Helium-Oxygen Diving To Depths Of 100 msw, Undersea Biomed. Res. 18, 66-67.*

54. *Nishi R.Y., 1989, Development Of New Helium-Oxygen Decompression Tables For Depths To 100 msw, Undersea Biomed. Res. 16, 26-27.*

55. *Paton W.D.M. and Walder D.N., 1954, Compressed Air Illness, Medical Research Council Report, HMSO 281, London.*

56. *Pease D.C. and Blinks L.R., 1947, Cavitation From Solid Surfaces In The Absence Of Gas Nuclei, J. Phys. Coll. Chem. 51, 556-567.*

57. *Pilmanis A.A., 1976, Intravenous Gas Emboli In Man After Compressed Air Ocean Diving, Office Of Naval Research Contract Report, N00014-67-A-0269-0026, Washington, DC*

58. *Plesset M.S. and Prosperetti A., 1977, Bubble Dynamics And Cavitation, Ann. Rev. Fluid Mech. 9, 145-185.*

59. *Powell M.R., Waligora J.M., Norfleet W.T. and Kumar K.V., 1993, Project Argo – Gas Phase Formation In Simulated Microgravity, NASA Technical Memo 104762, Houston.*

60. *Rashbass C., 1955, New Tables, Investigation Into The Decompression Tables, 243 Medical Research Council Report, UPS 151, London.*

61. *Schreiner H.R. and Hamilton R.W., 1987, Validation Of Decompression Tables, Undersea And Hyperbaric Medical Society Publication 74 (VAL), Bethesda.*

62. *Sears F.W., 1969, Thermodynamics, Reading: Addison Wesley Publishing Company.*

63. *Shapiro A.H., 1958, Dynamics And Thermodynamics Of Compressible Fluid Flow, New York: Ronald.*

64. *Sheffield P.J. and Vann R.D., 2002, Flying After Recreational Diving, DAN Workshop Proceedings, Durham.*

65. *Skripov V.P., 1974, Metastable Liquids, New York: John Wiley And Sons Incorporated.*

66. *Smith K.H. and Stayton L., 1978, Hyperbaric Decompression By Means Of Bubble Detection, Office Of Naval Research Report, N0001-469-C-0402, Washington DC*

67. *Spencer M.P., 1976, Decompression Limits For Compressed Air Determined By Ultrasonically Detected Blood Bubbles, J. Appl. Physiol. 40, 229-235*

68. *Strauss R.H., 1974, Bubble Formation In Gelatin: Implications For Prevention Of Decompression Sickness, Undersea Biomed. Res. 1, 169-174.*

69. *Strauss R.H. and Kunkle T.D., 1974, Isobaric Bubble Growth: Consequence Of Altering Atmospheric Gas, Science 186, 443-444.*

70. *Thalmann E.D., 1986, Air-Nitrox Decompression Computer Algorithm Development, USN Experimental Diving Unit Report, NEDU 8-85, Panama City.*

71. *Thalmann E.D., 1985, Development Of A Decompression Algorithm For Constant 0.70 ATA Oxygen Partial Pressure In Helium Diving, USN Experimental Diving Unit Report, NEDU 1-85, Panama City.*

72. *Kislyakov Y.Y. and Kopyltsov, 1988, The Rate Of Gas Bubble Growth In Tissue Under Decompression, Respir. Physiol. 71, 299-306.*

73. *Van Liew H.D. and Hlastala M.P., 1969, Influence Of Bubble Size And Blood Perfusion On Absorption Of Gas Bubbles In Tissues, Resp. Physiol. 24, 111-121.*

74. *Van Liew H.D., Bishop B, Walder P.D., and Rahn H., 1975, Bubble Growth And Mechanical Properties Of Tissue In Decompression, Undersea Biomed. Res. 2, 185-194.*

75. *Vann R.D. and Gerth W.A., 1997, Probabilistic Gas And Bubble Dynamics Models Of Decompression Sickness Occurrence In Air And Nitrogen-Oxygen Diving, Undersea Hyper. Med. 24, 275-292.*

76. *Vann R.D., Gerth W.A., and Leatherman N.E., 1987, A Likelihood Analysis Of Experiments To Test Altitude Decompression Protocols For SHUTTLE Operations, Aviat. Space Environ. Med. 58, A106-A109.*

77. *Vann R.D., Grimstad J., and Nielsen C.H., 1980, Evidence For Gas Nuclei In Decompressed Rats, Undersea Biomed. Res. 7, 107-112.*

78. *Vann R.D. and Clark H.G., 1975, Bubble Growth And Mechanical Properties Of Tissue In Decompression, Undersea Biomed. Res. 2, 185-194.*

79. *Walder D.N., 1968, Adaptation To Decompression Sickness In Caisson Work, Biometeor. 11, 350-359.*

80. *Wienke B.R. and O'Leary T.R., 2007, On A Dual Phase Bubble Model And Coupled Data Bank With Statistical Correlations And Risk Analyses For Selected Mixed Gas Dive Tables, Meters, And Profiles (accepted for publication Int. J. Biomed Sci.)*

81. *Wienke B.R., 2001, Basic Decompression Theory And Application, Flagstaff: Best Publishing Company.*

82. *Wienke B.R., 1992, Numerical Phase Algorithm For Decompression Computers And Application, Comp. Biol. Med. 22, 389-406.*

83. *Wienke B.R., 1991, Bubble Number Saturation Curve And Asymptotics Of Hypobaric And Hyperbaric Exposures, Int. J. Biomed. Comp. 29, 215-225.*

84. *Wienke B.R., 1990, Reduced Gradient Bubble Model, Int. J. Biomed. Comp. 26, 237-256.*

85. *Wienke B.R., 1989, Equivalent Multitissue And Thermodynamic Decompression Algorithms, Int. J. BioMed. Comp. 24, 227-245.*

86. *Wienke B.R., 1989, Tissue Gas Exchange Models And Decompression Computations: A Review, Undersea Biomed. Res. 16, 53-89.*

87. *Wienke B.R., 1987, Computational Decompression Models, Int. J. BioMed. Comp. 21, 205-221.*

88. *Wienke B.R., 1986, DECOMP: Computational Package For Nitrogen Transport Modeling In Tissues, Comp. Phys. Comm. 40, 327-336.*

89. *Yount D.E. and Hoffman DC, 1986, On The Use Of A Bubble Formation Model To Calculate Diving Tables, Aviat. Space Environ. Med. 57, 149-156.*

90. *Yount D.E., 1982, On The Evolution, Generation, And Regeneration Of Gas Cavitation Nuclei, J. Acoust. Soc. Am. 71, 1473-1481.*

91. *Yount D.E., 1979, Skins Of Varying Permeability: A Stabilization Mechanism For Gas Cavitation Nuclei, J. Acoust. Soc. Am. 65, 1431-1439.*

92. *Zeldovich J.B., 1943, On The Theory Of New Phase Formation: Cavitation, Acta Physiochimica, 18, 1-22.*

Figure 1. Flow Cavitation

Flow cavitation increases with small fluid vapor and ambient pressure differences, and with increasing fluid velocity and density. Euler first introduced a flow cavitation index, κ. Pressure reductions in vortex regions of rotational flow support void formation. Periodic formation and collapse of cavitation bubbles ie termed cloud cavitation, and occurs in fluctuating flows. Wakes behind high speed flows often fill with vapor, or gas, in a process called sheet cavitation. Lifting foils in air and water experience voids along the lifting surface, an extended bubble region. Frictional stress is a candidate mechanism for void structures in moving muscle. Radiation passing through material deposits kinetic energy along pathlengths, ionizing the media and producing separation voids. The index. κ, is given by,

$$\kappa = 2\,\frac{p - p_c}{\rho u^2}$$

with p and p_c, fluid static and vapor (plus gas) pressure, ρ, fluid density, and, u, fluid velocity. For flowing water, at STP roughly, the onset of cavitation occurs at flow speed, u_c, roughly 15 m/sec.

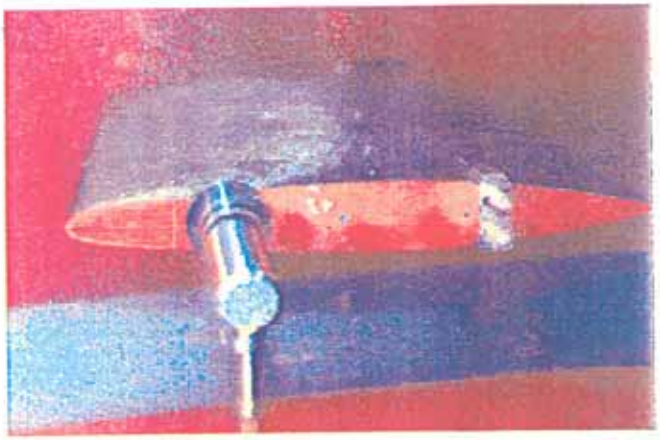

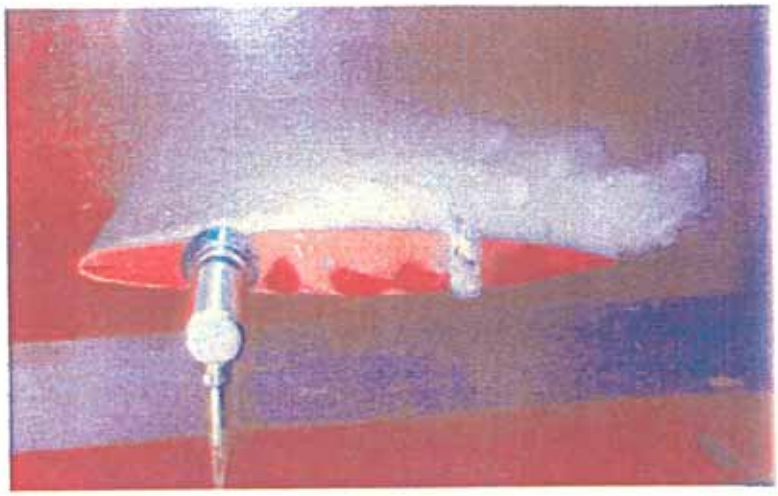

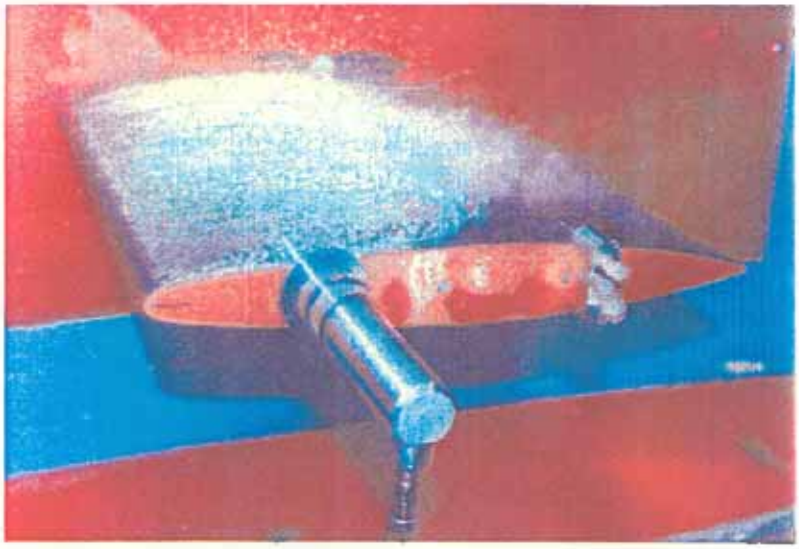

Figure 2. Plesset Inhomogeneous Nucleation

The nucleation center consists of a solid hydrophobic sphere of radius, r_0, and the Gibbs probability is calculated for a vapor phase to develop within a concentric shell extending from seed radius, r_0, to larger radius, r. The probability for nucleation depends on the surface tensions, γ_{lv}, γ_{vs}, and γ_{ls}, associated with the liquid-vapor, vapor-solid, and liquid-solid interfaces, noted by θ, the contact angle. For hydrophobic surfaces, θ is large, approaching 180^o, while for hydrophilic surfaces, θ is small, nearing 0^o.

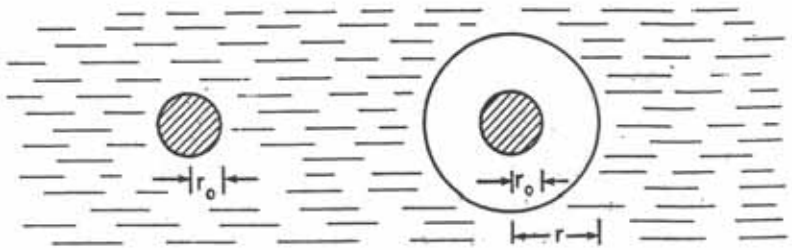

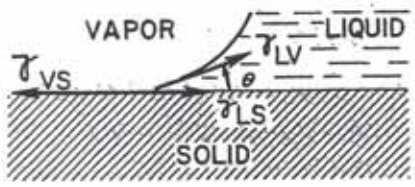

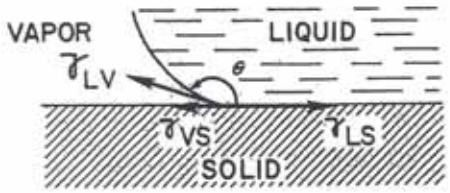

Figure 3. Gibbs Free Energy Versus Critical Radius

The critical radius of a droplet increases as the amount of supercooling or superheating, ΔT, decreases. The barrier height also grows with smaller ΔT.

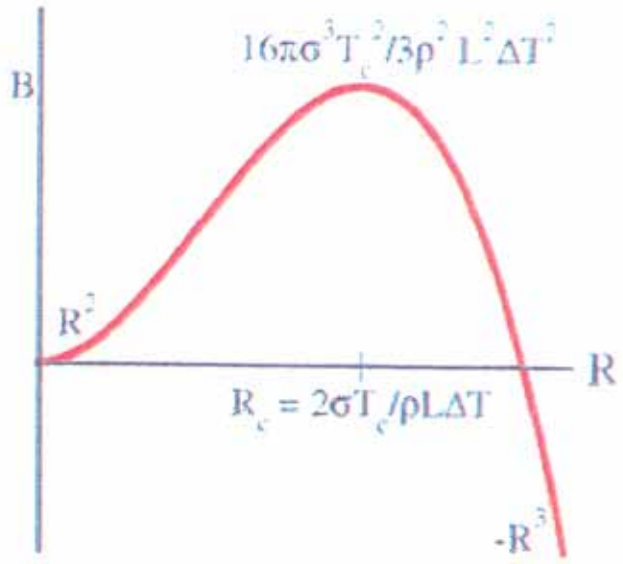

Figure 4. Bubble Flow Distortion

Deviations from sphericity for bubbles increase with flow speed in a fluid. Below are depicted deviations from sphericity (icons) for a rising bubble in a water column. The diagonal line denotes the transition domain as a function of Reynolds number versus Eotvos number.

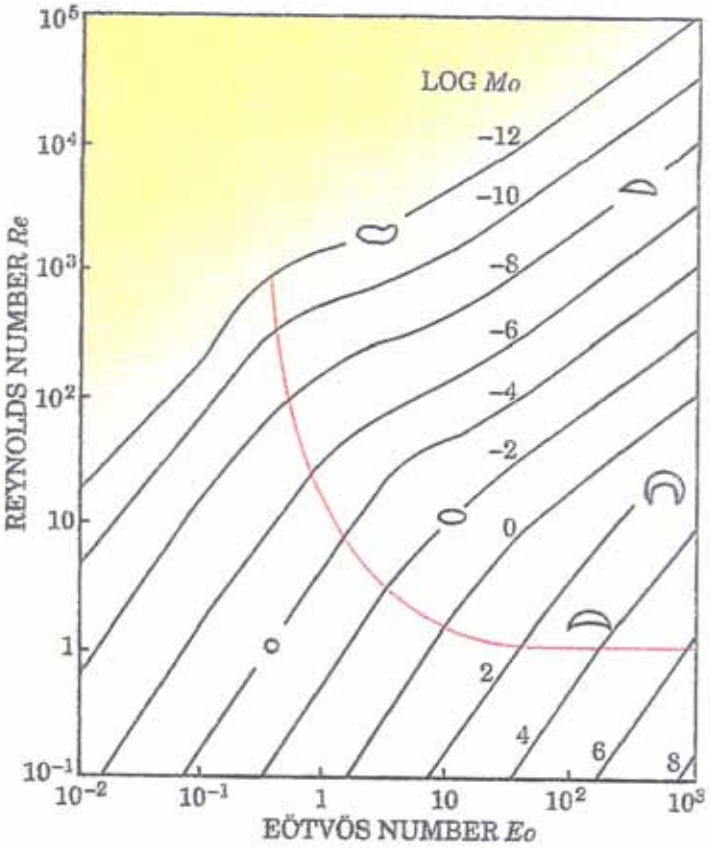

Figure 5. Two Bubble Flow With Free Surfaces

Two bubbles beneath a free surface present a challenging computational problem for the Rayleigh-Plesset equation. Numerical solution on fine 3D meshes can only be effected with high speed computers. Even mesh generation requires supercomputers.

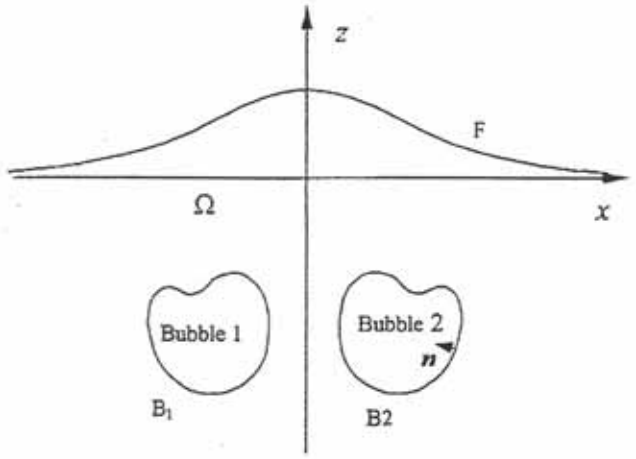

. Geometry and coordinate system used to model the interaction among two gas bubbles and a free surface.

Level 1 Level 8

. Level 1 and 8 of the triangulation of a sphere.

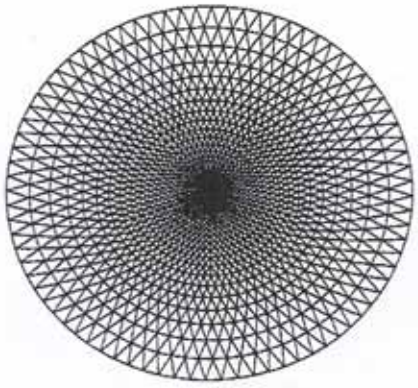

. Level 16 of the triangulation of a free surface.